Contents lists available at ScienceDirect

Carbohydrate Polymers

journal homepage: www.elsevier.com/locate/carbpol

Magnetic field-assisted aligned patterning in an alginate-silk fibroin/nanocellulose composite for guided wound healing

Keya Ganguly [a,1], Hexiu Jin [d,1], Sayan Deb Dutta [a,1], Dinesh K. Patel [c], Tejal V. Patil [a,b], Ki-Taek Lim [a,b,*]

[a] Department of Biosystems Engineering, Kangwon National University, Chuncheon 24341, Republic of Korea
[b] Interdisciplinary Program in Smart Agriculture, Kangwon National University, Chuncheon 24341, Republic of Korea
[c] Institute of Forest Science, Kangwon National University, Chuncheon 24341, Republic of Korea
[d] Department of Plastic and Traumatic Surgery, Capital Medical University, Beijing 10069, China

ARTICLE INFO

Keywords:
Cellulose nanocrystals
Magnetic field
Alignment
Scaffold
Re-epithelialization
Wound healing

ABSTRACT

This study was focused on utilizing the magneto-responsiveness of cellulose nanocrystals (CNCs) in an alginate-silk fibroin (ASF) matrix under a low-strength (0.28 T) magnetic field (MF) for fabrication of a magnetically aligned, anisotropic, three-dimensional wound healing scaffold. The effect of the MF on three different concentrations of CNCs (0.5%, 1%, and 2%) was studied to control the alignment of the ASF scaffold. The as-fabricated scaffolds exhibited a concentration-dependent anisotropy with respect to the CNCs. The SEM, AFM, and, SAXS analysis indicated a higher degree of anisotropy of the MF-treated scaffolds with significant enhancement of Young's modulus vis-à-vis control, demonstrating their mechanical stability. Skin fibroblasts, keratinocytes, and endothelial cells cultured on the magnetically aligned scaffolds showed enhanced proliferation *in vitro* and demonstrated rapid wound closure under *in vivo* conditions. Hence, the magnetic property of CNCs could be useful for developing biomimetic anisotropic constructs for wound healing applications.

1. Introduction

Nearly 2.5% of the total population in the United States and most developing countries suffers from chronic wounds (Sen, 2021). The financial burden of treating injuries is an alarming consequence of increasing healthcare costs. Hence, prioritization of wound care research has become a compelling need to maintain healthy quality of life of patients. Moreover, the National Institutes of Health (NIH) Research Portfolio Online Reporting Tools (RePORT) has listed wounds as a significant category of current challenges (Sen, 2019). Traditional wound dressings such as bandages, cotton, and gauzes fail to provide an appropriate environment for wound healing (Farahani & Shafiee, 2021; Rezvani Ghomi et al., 2019; Kus & Ruiz, 2020). As a promising alternative, skin tissue engineering is a research area that is rapidly expanding toward restoring cellular functions, re-epithelialization, and vascularization in wounded tissue for effective public healthcare (Nour et al., 2021). One of the ideal tissue engineering approaches to healing damaged skin tissue is the implantation of biomimetic scaffolds that provide favorable three-dimensional (3D) geometry resembling the skin tissue extracellular matrix (ECM) to promote dermal, epidermal, and angiogenic growth.

Many scaffold-guided wound healing platforms have been designed to achieve impressive repair of wounded tissue (Wu et al., 2021). A few key features of these scaffolds are excellent mechanical properties, high porosity, flexibility, and ECM-mimicking geometry (Negut et al., 2020; Xing & Tang, 2021). Among such new dressings, biopolymers capable of transforming into 3D shapes in response to external stimuli have attracted much attention (Zarket et al., 2021; Lavrador et al., 2021; Zhou, Vázquez-González, & Willner, 2021; Gelmi & Schutt, 2021). In particular, the external magnetic field (MF) is an extensively studied stimulus for controlling scaffold topologies, including microstructural patterns and anisotropic alignments (Farzaneh et al., 2021; Onbas & Arslan Yildiz, 2021; Huang et al., 2020). An integrated system of a superparamagnetic scaffold along with MF stimulation of 10 mT was designed by Hao et al. to improve the wound healing efficiency of fibroblasts. The magneto-responsiveness of the scaffold was used to transfer the MF-induced mechanical cues to biochemical changes in the fibroblasts through the activation of components of integrin, focal

* Corresponding author at: Department of Biosystems Engineering, Kangwon National University, Chuncheon 24341, Republic of Korea.
E-mail address: ktlim@kangwon.ac.kr (K.-T. Lim).
[1] Contributed equally.

https://doi.org/10.1016/j.carbpol.2022.119321
Received 29 November 2021; Received in revised form 10 February 2022; Accepted 3 March 2022

adhesion kinase, and extracellular signal-regulated kinase signaling pathways (Hao et al., 2018). MF stimulation of ~7 T has been used to fabricate a corneal stroma-like scaffold composed of numerous orthogonal layers of oriented collagen I fibrils for the *in vitro* culture of human corneal keratinocytes *via* a contact guidance mechanism to achieve corneal re-epithelialization, transparency, and neovascularization (Builles et al., 2010; Torbet et al., 2007). MF-responsive ferrogels with tunable mechanical properties under MF stimulation as low as 200 mT have also been developed to mimic the contractile forces found in biological systems; they demonstrated on-demand adaptive mechanical properties on epithelial cells (MCF10A) (Chen et al., 2021). A magnetic nanohybrid of polydopamine-iron oxide nanoparticles-montmorillonite (PDA-Fe_3O_4-MMT) was aligned inside a polyvinyl alcohol/polyacrylic acid (PVA/PAA) hydrogel matrix under MF stimulation of 40 mT to enhance the mechanical properties (compressive strength ~4.86 MPa) of the gel for biological applications (Chen, Zhang, et al., 2022). Anisotropic topographic features at the submicron scale in an alginate (Alg) scaffold have been demonstrated under an MF of 0.24 T and low-temperature conditions. The physiological effect of the designed anisotropy was tested on mouse myoblasts (C2C12). The C2C12 cells cultured on the magnetically aligned scaffold demonstrated co-oriented morphology in the direction of the magnetic alignment (Margolis et al., 2018).

Cellulose nanocrystal (CNC)-reinforced polymer composites have also gained attention owing to the inherent molecular orientation (C—C, C—O, C—H, and –OH interactions) within individual CNCs, which are responsive to MF stimulation (Shen et al., 2020; Abitbol & Cranston, 2014; Sugiyama et al., 1992; De France et al., 2016). Some pioneering works have used this property of CNC directional alignment to control the alignment of starch-based polymer matrices (Babaei-Ghazvini et al., 2020; Frka-Petesic et al., 2017) and to improve the hydromechanical performance of nanocomposites for prospective tissue engineering applications (Wang et al., 2015). Fe_3O_4-doped magnetic CNCs have also been investigated for the fabrication of anisotropic nanocomposites with polylactic acid (PLA) for high-performance engineered biomimetic structures (Dhar et al., 2016).

Despite the numerous reports on the fabrication of bioactive scaffolds based on the magneto-responsiveness of CNCs, the fabrication of an anisotropic scaffold mimicking the anisotropy of the skin is yet to be researched extensively. Additionally, the physiological response of co-cultured skin cells of the epidermis, dermis, and endothelium on a magnetically aligned CNC-containing scaffold remains unstudied. Combining the magneto-responsiveness of CNCs with the bioactive cues of biopolymers might enhance the bulk properties of the nanocomposite as a wound dressing. Among the several polymer matrices, alginate (Alg) is a reliable biopolymer for wound repair (Rezvanian et al., 2021). It has been reported to absorb wound fluid and form gels that provide a physiologically moist environment, thereby promoting rapid re-epithelialization and granulated tissue formation (Varaprasad et al., 2020). Silk fibroin (SF) has also shown remarkable efficiency as a wound dressing agent owing to its unique properties such as high biocompatibility, slow degradation, low immunogenicity, high water absorption capacity, excellent air permeability, cost-effectiveness, and suitable mechanical properties (Farokhi et al., 2018; Naomi et al., 2020; Park et al., 2018; Martínez-Mora et al., 2012; Park et al., 2005; Liu et al., 2010).

Our aim was to evaluate CNC-induced regulation of scaffold topology in an Alg-SF-CNC nanocomposite under MF stimulation for rapid wound healing. We hypothesized that a low-strength magnetic field (0.28 T) could be applied to effectively control the topology of the CNC-reinforced nanocomposite for guided wound healing. The fabricated scaffolds were analyzed for their chemical and biological properties. The healing efficiency of the scaffold topology obtained in the *in vitro* studies on dermal fibroblasts (HDFs), keratinocytes (HaCaT), and endothelial cells (HUVECs) was also confirmed in an *in vivo* subcutaneous wound model. To the best of our knowledge, this is the first report of low-strength MF-induced alignment in an Alg-SF-CNC matrix for the co-culture of epidermal, dermal, and endothelial cells (HDFs, HaCaT, and HUVEC cells) for topology-guided wound healing applications (Scheme 1). We anticipate that the magneto-responsiveness of this CNC-based tissue engineering scaffold would be vital in engineering 3D scaffolds mimicking the skin anisotropy for clinical applications.

2. Materials and method

2.1. Materials and reagents

Cellulose nanocrystals from Rice husk (CNCs, 10–20 nm width, 50–400 nm length) were synthesized as previously reported (Patel et al., 2021). Calcium chloride anhydrous (Purity ≥93.0%), silk fibroin (SF), and sodium alginate from brown algae (Purity ≥98.0%) were purchased from Sigma-Aldrich St. Louis, MO, USA. Dulbecco's Modified Eagle's Medium (DMEM), 10% fetal bovine serum (FBS), Dulbecco's phosphate-buffered saline (DPBS), and antibiotics were purchased from Welgene Inc., Republic of Korea. Trypsin-ethylene diamine tetra acetic acid (Trypsin-EDTA) was provided by Gibco, USA. WST-8 EZCytox Cell Viability Assay Kit® was purchased from DoGenBio Co., Ltd., Republic of Korea. Acridine orange, Ethidium bromide stains, Propidium iodide RNaseA staining buffer (PI), and TRIzol® reagent were purchased from Invitrogen, Thermo Fisher Scientific, USA. The cDNA synthesis kit was obtained from Invitrogen, Gaithersburg. The gene primers were supplied by BIONEER®Inc., Daejeon, Republic of Korea. SYBR Green Master mix was provided by Bio-Rad Laboratories, USA. Bovine Serum Albumin (BSA), Hexamethyldisilazane (HMDS), paraformaldehyde (PFA), 4,6-diamino-2-phenylindole dihydrochloride (DAPI), and hematoxylin stain were acquired from Sigma-Aldrich, USA. Alexa Fluor conjugated monoclonal antibodies were purchased from Santa Cruz Biotechnology, USA. Vascular endothelial growth factor (VEGF) and Epidermal growth factor (EGF) were obtained from GenScript, USA. Human growth factor array C1 and Human phosphorylation multi-pathway profiling array C55 were purchased from RayBiotech, USA.

2.2. Magnetic field

The MFs were generated by a neodymium iron boron (NdFeB) magnet (50 × 50 × 5 mm^3, NEOMAX, Sumitomo Co., Osaka, Japan) with an average flux density of 0.48 ± 10 T. The flux density was measured by a Tesla meter (Tesla meter, model TM-801.EXP, Kanetec Co. Ltd., Tokyo, Japan) at the bottom and top of each magnet disk. The magnetic field stimulation was applied on polymer solution cast onto a 4 well plate in between the magnets at a distance of 1 cm at room temperature (RT), generating an MF strength of 0.28 T around the sample. The list of MF exposure conditions and the composition of the scaffolds are listed in Table S1.

2.3. Scaffold fabrication

Four different categories of scaffolds were fabricated. Namely, Alginate-Silk fibroin (ASF) and ASF incorporated with 0.5%, 1%, and 2% CNCs (ASC 0.5, ASC 1, and ASC 2), respectively. Among these, ASF was taken as the control while the rest served as the experimental group. For the scaffold fabrication, a homogenous aqueous solution of CNC was first prepared to obtain a final concentration of 0.5%, 1%, and 2% (*w/v*) for 20 mL of polymeric solution. Simultaneously, an aqueous solution of Na-alginate was prepared (3 *w/v*%) and heated at 70 °C for 2 h with constant stirring until proper gelation. Next, the pre-prepared aqueous solution of CNC was added according to the desired concentrations and stirred overnight to ensure homogenous dispersion. Following this, the temperature of the solution was dropped to 37 °C, and calculated amounts of SF (0.05 *w/v*%) were mixed continuously in the solution for 1 h. An equal amount of each solution was cast onto 4 well-plates for a MF stimulation of 8 h. A similar set was cast to fabricate the

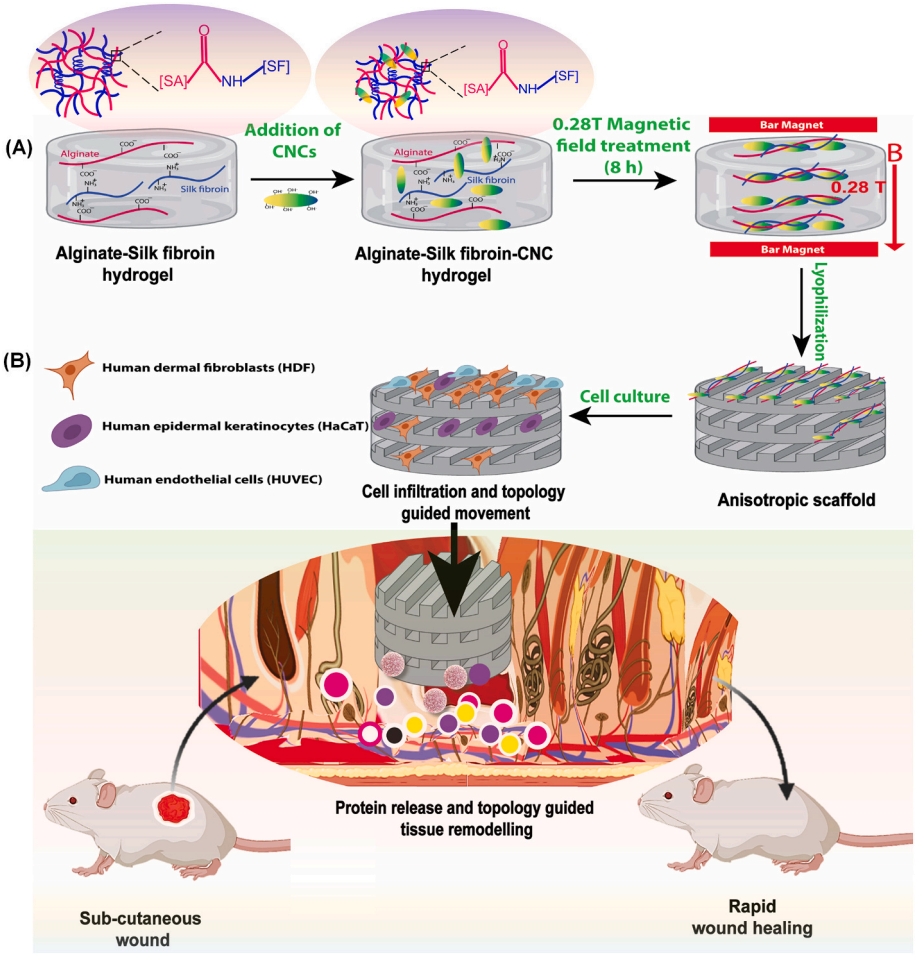

Scheme 1. **(A)** Schematic of the preparation of anisotropic scaffold of alginate, silk fibroin, and cellulose nanocrystals (CNCs) in the presence of low-intensity magnetic field (MF). **(B)** CNCs directed aligned patterning promote rapid cell infiltration, protein release, and topology guided wound healing.

unstimulated counterpart. Finally, the gels w/wo magnetic bars were transferred to −70 °C for 24 h followed by lyophilized for 48 h. All the fabricated scaffolds were UV sterilized before the experiments.

2.4. Scaffold characterizations

2.4.1. Morphological characterization

The diameter and the thickness of the fabricated scaffolds were measured using a Vernier caliper (A&D company limited, AD-5764A-200, Tokyo, Japan) at ten randomly selected points in triplicate samples. The morphology of the fabricated scaffolds was analyzed by a scanning electron microscope (UR-SEM, Hitachi-S4800, California, USA) with an acceleration voltage of 15.0 kV/cm. The surface topology was evaluated using atomic force microscopy (AFM, Nanoscope 5 Bruker, USA) through drop-casting of the fabricated samples w/wo MF stimulation. The morphology of the CNCs was monitored by ultrahigh-resolution transmission electron microscopy (UHR-TEM; AARM 1300S, Jeol, Japan) with a resolution of 0.12 nm.

2.4.2. Interaction and crystallinity study

The Perkin Elmer FTIR analyzer (Frontier, Perkin Elmer, UK) was used to evaluate the functional groups present in the sample in a transmitted mode in the wavenumber range of 4000–1000 cm^{-1} with a resolution of 4 cm^{-1}. The X-ray diffraction (XRD) patterns of the fabricated samples were obtained at ambient temperature on an X'Pert PRO X-ray diffractometer (X'Pert PRO MPD, Philips, Eindhoven, Netherlands) at an operating voltage (40 kV) and current (40 mA) with Cu K_α radiation (λ = 1.5414 Å). The operating range (2θ) was 5–40°. The nanostructure of the fabricated scaffolds was also determined using SAXS analysis with Xeuss 2.0 system at a sample-to-detector distance of 2500 mm. The samples were exposed for 600 s for individual measurements. The intensity *vs* scattering vector was analyzed along with the respective 2D patterns and azimuthal angles. The orientation of the 2D patterns were quantified with the eccentricity (*E*) by taking the scattering patterns as ellipses using the following formula,

$$e = \sqrt{1 - \frac{b^2}{a^2}}$$

where, 'b' denotes the ellipse minor axis while 'a' denotes the ellipse major axis.

2.4.3. Mechanical testing

Compression testing was performed on a MCT-1150 (A&D, Japan) instrument with a test speed of 10 mm/min. Young's modulus for each sample was calculated by determining the slope of the linear region of the stress-strain curve (strain region of 3–5%) while the toughness was measured from the area under the stress- strain curve.

2.4.4. Rheological characterization

The rheological analysis was carried out using an ARES-G2 rheometer (TA Instruments, New Castle, Delaware, USA) with a 6 mm parallel plate. The hydrogels were characterized by flow and temperature sweeps at 30 °C and 35 °C. The hydrogel without CNC was considered as the control group.

2.4.5. Swelling and BSA release study

The swelling test was conducted to evaluate the hydrophilic-hydrophobic behavior of the fabricated scaffolds. For this, the dry weight of a certain amount of each scaffold was recorded (W_d). Next, the samples were immersed in 2 mL PBS at 37 °C under static conditions. The scaffolds were then blotted, and the swollen weight of each sample was recorded (W_s) at different time intervals (0, 0.5, 1, 21, 3, 4, 5, 6, 12, 24, 48 h) until equilibrium swelling was reached. The swelling ratio was calculated according to the following equation.

$$\%swelling = \left(\frac{W_s - W_d}{W_d}\right) \times 100\%$$

BSA was incorporated into the fabricated scaffolds as reported earlier with slight modification (Yu et al., 2015). Briefly, the equal weight of each scaffold was immersed in 1 mL of PBS containing 20 mg/mL BSA and incubated for 1 h at RT on a shaker. After incubation, the supernatant was collected, and the excess BSA was washed with PBS. The scaffolds were then freeze-dried, and the BSA loading was determined as the difference between the final weight and the initial weight of the scaffolds. Next, the BSA-loaded scaffolds were immersed in 1 mL of PBS at RT under shaking conditions to analyze the BSA release profile. 100 μL of PBS was withdrawn at different time intervals and stored at −20 °C until the final test. The withdrawn PBS was replenished by fresh PBS. BSA release was quantified using the colorimetric BCA protein quantification assay kit (Amplite™, AAT Bioquest, USA).

2.5. In vitro biocompatibility assay

HDF (ATCC No. PCS-201-012), HaCaT (ATCC No. PCS-200-011), and HUVEC (ATCC No. PCS-100-010) were maintained in DMEM containing 10% FBS and 1% P/S antibiotics at 37 °C in a humidified atmosphere containing 5% CO_2 (Steri-Cycle 370 Incubator; Thermo-Fischer Scientific, USA). The cytotoxicity of the fabricated scaffolds was performed using the WST-8 assay and Live-Dead assay procedure.

For WST-8 assay, the individual cultures of HDF, HaCaT, and HUVEC (1×10^4 cells/100 μL media) and co-culture of HDF, HaCaT, and HUVEC (1×10^4 cells each/100 μL media) were seeded into a 96-well plate w/wo the fabricated scaffolds (ASF, ASC 0.5, ASC 1, and ASC 2) and cultured for 1, 3, and 5 days. The cells seeded onto TCPS without scaffold were considered as control. After the indicated time intervals, 10 μL of the WST-8 dye was added and incubated for 2 h. The produced formazan was quantitated by measuring the absorbance at 450 nm (625 nm as a reference value).

For live/dead staining, each of the HDF, HaCaT and HUVEC (1×10^4 cells each/100 μL media) were co-cultured with the fabricated scaffolds (ASF, ASC 0.5, ASC 1, and ASC 2) for 1, 3, and 5 days. The cells were washed with 1× PBS, followed by treatment with 1 μL of acridine orange and ethidium bromide dye solution at a ratio of 1:1. The images were captured immediately on appropriate filter channels using Leica Microsystems Suite X software (Leica Microsystems, Germany) of the inverted fluorescence microscope (DMi8 Series, Leica Microsystems, Germany). The survivability of the treated cells was quantified using the live-dead fluorescence imaging after 3 days of incubation.

2.6. Cell cycle distribution analysis

Cell cycle analysis was performed using PI staining, as reported earlier with slight modification (Han et al., 2018). Briefly, the scaffold-treated cells were trypsinized after 24 h and washed twice with PBS by centrifugation. The obtained cell pellet was resuspended in 1 mL ice-cold PBS and fixed overnight in 9 mL of 70% ice-cold ethanol. Next, the fixed cells were treated a 300 μL RNase A-PI solution at 37 °C for 30 min. The cell cycle was analyzed by a flow cytometer (FACS Calibur, BD Biosciences, San Jose, USA), and data were analyzed by BD CellQuest Pro software (BD Biosciences, USA). The percentage of cells at Sub-G0/G1, G0/G1, S, and G2/M phases were calculated and compared with the control groups.

2.7. Morphological analysis of the cultured cells

2.7.1. Immunocytochemical analysis

The arrangement of F-actin and paxillin was studied through fluorescence imaging to visualize the effect of the scaffold on the cell cytoskeleton. The HDF, HaCaT, and HUVEC (1.5×10^4 cells/100 μL media) were individually cultured in 60 mm bottom well plates for 3 days. The staining of cells was performed at RT unless specified. Briefly, the cells were washed with PBS, fixed with 3.7% PFA for 15 min, and permeabilized with 0.1% Triton X-100 for 10 min. The permeabilized cells were then rinsed twice with PBS and blocked for 1 h with 1% BSA. After this, the cells were incubated for 1 h with 200 μL mouse anti-human paxillin (ex/em = 488/520) at a dilution of 1:300 in BSA. Next, the cells were incubated for 30 min with a 200 μL Alexa Fluor (AF) 555 F-actin probe (ex/em = 553/568) to visualize the F-actin. The nuclear staining was done with the addition of 20 μL of 1 mg/mL DAPI solution for 2 min in the dark. The stained cells were rinsed and covered with a mounting medium and a glass coverslip. The fluorescence images were taken with a fluorescence microscope at a magnification of 40×.

2.7.2. SEM morphology

The morphology and cell adhesion were also evaluated using SEM. For this, the HDF, HaCaT, and HUVEC (0.5×10^4 cells each/100 μL media) were co-cultured for three days. After this, the culture medium was removed. The samples were fixed for SEM analysis with 3.7% PFA for 15 min at RT. After that, samples were dehydrated in a series of ethanol solutions (30%, 50%, 70%, 80%, 90%, and 100%) for 15 min each. Finally, dehydrated samples were immersed in HMDS under a fume hood for 5 min, washed twice with distilled water, and left to dry overnight.

2.7.3. Hematoxylin staining

The distribution of cells in the fabricated scaffold was analyzed using the hematoxylin staining procedure after 3 days of co-culture. Briefly, the co-cultured cells were fixated with 4% PFA for 24 h. The fixed cells were washed with PBS and serially dehydrated with 50%, 70%, 90%, and 100% ethanol for 5 min each. Following this, the cells were stained with hematoxylin for 1 min and washed thoroughly with DW for 10 min. The images were captured at the magnification of 10× under an optical microscope (Zeiss Optical Microscope, USA).

2.8. Determination of cell migration

The cell migration assay was performed using a transwell chamber (6.5 mm insert, 8.0 μm-pore polycarbonate filters, Transwell® Permeable Support, Costar, USA). Briefly, 250 μL cell suspension of HDF, HaCaT, and HUVEC at 1:1:1 ratio in serum-free DMED media (with 1% PS) was cultured into the upper well of a transwell plate. The lower chamber was filled with 750 μL of DMEM containing experimental samples (ASF, ASC 0.5, ASC 0.5 supplemented with 500 ng VEGF, ASC0.5 supplemented with 500 ng VEGF/EGF) for 12 and 24 h. ASF containing medium was taken as the control set. Following incubation, the number of migrated cells in the transwell insert was fixed with 3.7% PFA for 5 min, permeabilized with 100% methanol for 20 min, and stained with Giemsa for 10 min. The excess stain was removed by washing with PBS, and images were captured at the magnification of 10× under an optical microscope (Zeiss Optical Microscope, USA).

2.9. RNA isolation and real-time PCR (qRT-PCR) analysis

The expression of the marker genes in scaffold treated cells was evaluated by the qRT-PCR technique. Briefly, the cells (4×10^4 cells/100 μL media) were cultured in a 24-well plate in the DMEM media for 7

and 14 days, followed by RNA extraction by TRIzol® reagent, according to the manufacturer's instructions. The purity and concentration of the extracted RNA were evaluated by a spectrophotometer. The cDNA was synthesized, and PCR was performed from 2 μg of RNA using reverse transcriptase and SYBR Green Master mix. The mRNA expression was quantified with a Bio-Rad Real-Time PCR (CFX96TM Maestro Real-Time System, Bio-Rad, USA). The reaction condition included 43 cycles of denaturation for 15 s at 95 °C and 1 min amplification at 60 °C. All the experiments were performed in triplicate and normalized to the housekeeping gene GAPDH. The relative mRNA expression from HDF, HaCaT, and HUVEC was compared in a histogram. The list of primers used is listed in Table S2.

2.10. Immunocytochemical staining of marker protein

The expression of the marker proteins was studied through an immunocytochemical staining procedure. The HDF, HaCaT, and HUVEC (4×10^4 cells/100 μL media) were cultured in 60 mm bottom well plates with scaffold and treated for 7 and 14 days. The staining of cells was performed by washing with PBS, followed by fixing with 3.7% PFA for 15 min at RT. Next, the cells were permeabilized by adding 0.1% Triton X-100 for 10 min at RT. After that, the cells were rinsed twice with PBS, blocked by 1% BSA, and incubated with 250 μL of mouse monoclonal antibodies against Fibronectin, Basic Cytokeratin, and PECAM. The nucleus was counterstained with 20 μL of 1 mg/mL DAPI solution for 2 min in the dark. The stained cells were rinsed and covered with a mounting medium and a glass coverslip. The fluorescence images were taken with a fluorescence microscope at a magnification of 40×.

2.11. Antibody array and bioinformatics studies

Following the manufacturer's instructions, a human growth factor antibody array was used to identify the growth factor expression profiles of co-cultured cell secretome. The Human phosphorylation multi-pathway profiling array was used to determine the changes in the signaling pathways in HDF only. Next, the densitometry data were obtained using ImageJ (National Institutes of Health, USA (http://imagej.nih.gov/ij/)) and used to compare different samples after background subtraction and normalization against positive control spots. The STRING (www.string-db.org) software was used to identify protein-protein interactions among the identified proteins. Additionally, we performed the functional enrichment analysis using gene ontology (GO).

2.12. In vivo studies

The *in vivo* study was conducted to determine the wound healing efficiency of the fabricated scaffolds. For this purpose, ICR male rats (total number of rats = 12, 42–52 g) were supplied with sufficient food and water for 4 days before surgery. The experiment was divided into three groups; negative control– without treatment, positive control– MF-treated pure polymer scaffold, and experimental group– MF-treated ASC 0.5 scaffold. We chose ASC 0.5 scaffold for the *in vivo* experimentation because of its effectiveness in the *in vitro* biological studies. Each group has duplicate rats with one experiment site. Briefly, the dorsal hair was removed and the skin surface was disinfected with 70% ethanol. Then, the animals were placed in a lateral position. A 10 mm diameter circular wound was created using a sterile biopsy punch to remove two layers of dorsal skin and create full thickness excisional wounds. All rats were placed in a protected and sound-proof room at 21 ± 1 °C and a relative humidity of 35 ± 1%. The room was maintained at 12 h light and 12 h dark cycle. The macroscopic wound healing analysis was conducted after 7 and 14 days post-surgery. For the histological analysis, the rats were sacrificed after 14 days post-surgery with utmost care to reduce animal suffering.

For the histological staining, the collected samples were fixed with 3.7% PFA solution for 2 days followed by decalcification with 12% ethylene diaminetetraacetic acid (EDTA) at 4 °C. The tissue samples were then cleaned and dehydrated in alcohol. The dehydrated samples were embedded in parafilm to produce fine section followed by staining with hematoxylin (H), eosin (E), and Masson's trichrome (MT). All surgical procedures were approved by the Institutional Animal Care and Use Committee (IACUC) of Capital Medical University. Beijing, China. The surgical procedures were approved by the Animal Experimental and Ethical Committee (Permission No. KQYY-202012-004).

2.13. Statistical analysis

Statistical analysis was performed using OriginPro 9.0 software. Statistical significance between the control and treatment groups was determined using one-way ANOVA. All the data are presented as mean ± SDs. Differences were considered significant at * $p < 0.05$, ** $p < 0.01$, and *** $p < 0.001$.

3. Results and discussion

3.1. Ultrastructural and topographical characterization

MF-treatment directs specific molecular interactions that lead to distinct particle clustering, chaining, attractions, and alignments in a magneto-responsive composite (Irons et al., 2021). A CFD model of the magnetic field strength (0.28 T) applied on our fabricated scaffolds is presented in Fig. S1. A non-homogeneous porous topology was observed in the control ASF scaffold under both conditions (w/wo MF) as shown in Fig. 1 (A1 & E1). Strikingly, a distinct aligned topology was obtained in the Alg-SF-CNC nanocomposites in the presence of a 0.28 T MF as evidenced in Fig. 1 (E1–H2), unlike in their respective counterparts without MF, Fig. 1 (A1–D2). At low magnification, the FE-SEM analysis indicated the appearance of distinct parallelly formed polymer walls in the MF-treated scaffolds for a CNC concentration as low as 0.5%. In contrast, scaffolds fabricated without MF-treatment induced weakly aligned polymer wall formation at a CNC concentration of 2%. A clear transition of the porous to weakly parallel alignment in the polymer matrix without MF-treatment was observed from ASF to ASC-2, which is most likely induced by freeze-drying. CNCs have previously been reported to affect the alignment in a polymer matrix upon freeze-drying in a concentration-dependent manner (Han et al., 2013). Our result indicates that the MF-stimulation has generated distinct parallel alignment in the CNC-containing scaffolds even at 0.5% CNC concentration. We anticipated that the distinct alignment in the fabricated scaffolds might have resulted from the local ordering of the CNCs under MF stimulation which was indicated by the SEM images at higher magnification. At a higher resolution, the scaffolds revealed distinct textures with long-range order (perpendicular to the applied MF) in the MF-treated CNC-containing scaffolds, as observed in Fig. 1 (F2–H2). The untreated counterparts revealed long-range angular orders to randomly organized nanostructure w.r.t. the magnetic field direction, as indicated in Fig. 1 (B2–D2). Moreover, to confirm that the CNCs used in scaffold fabrication acted as individual dipoles at the nanoscale under the MF-stimulation, we checked their alignment in aqueous dispersion medium. The morphological aspect analyzed using UHR-TEM of the CNCs (~115 ± 80 nm in length and 17 ± 4.5 nm in breadth), and their orientation, analyzed using AFM, under the effect of a 0.28 T magnetic field are shown in Fig. S2 (A & B). Random orientation of CNCs was observed in the control set without the application of MF. However, distinct alignment of the CNCs was observed under the effect of MF, confirming the magnetic field responsiveness of individual CNCs, most likely as nanomagnets. Furthermore, the CNC containing polymer precursor was drop casted w/wo MF-treatment to determine topological changes through AFM analysis. Figs. S3 and S4 represent the 2D AFM images of the fabricated scaffolds W/ WO MF-treatment, along with their corresponding line scans and height profiles, respectively. We observed distinct ridge and grooves in the MF-treated samples compared

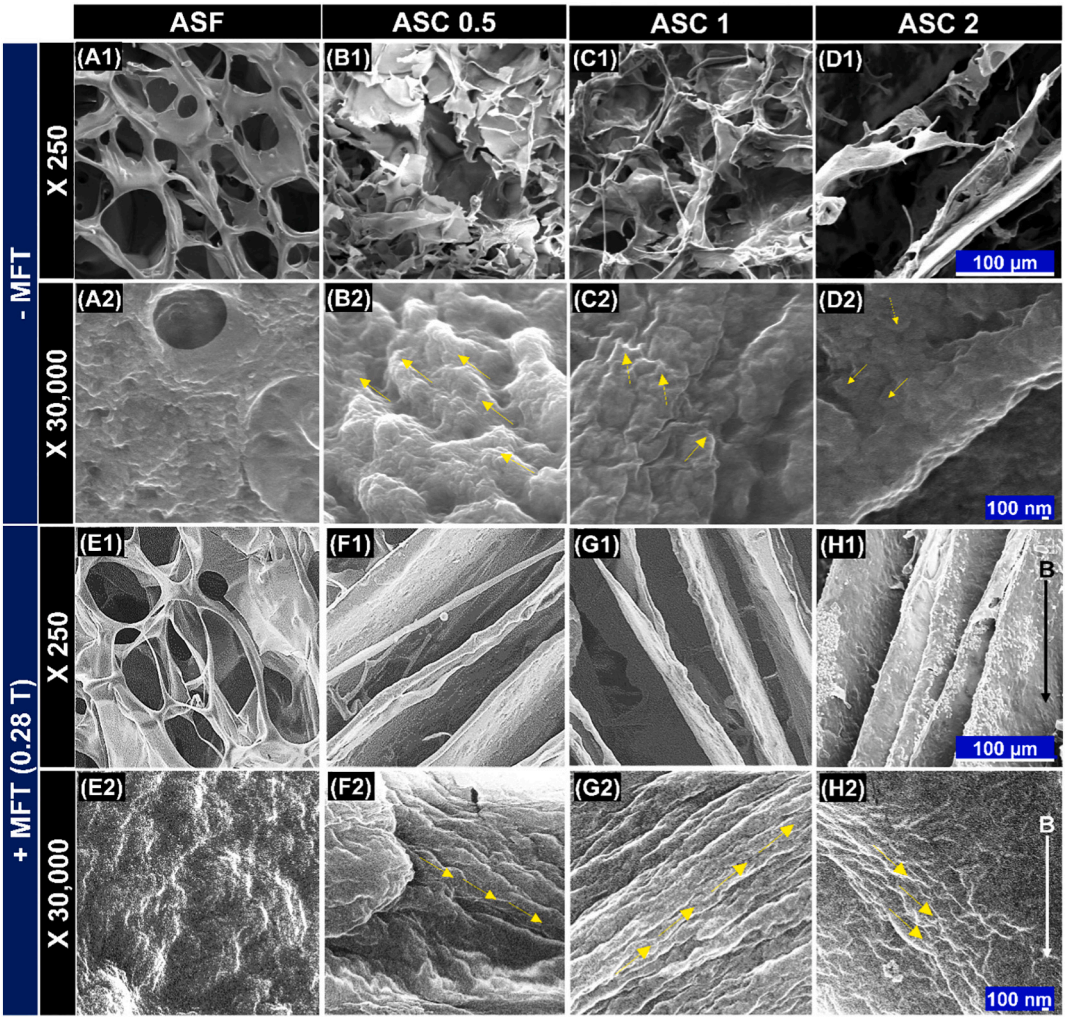

Fig. 1. Effect of magnetic field on the topology of fabricated scaffolds. FE-SEM images of freeze-dried ASF and its composite scaffolds (A1-D2) without and (E1-H2) with MF-treatment. The yellow arrows indicate the direction of well-defined nano structures. The white and black arrow indicates the direction of the applied magnetic field 'B'. Scale bar: 100 nm and 100 µm. (For interpretation of the references to colour in this figure legend, the reader is referred to the web version of this article.)

to the untreated set, consistent with the SEM images. ASF shows a maximum height profile of ~20 nm and a periodicity of 3 µm between the grooves, and ~25 nm peak-to-valley height differences. With an increase in CNC concentration, the peak-to-valley height increased from ~60 nm in ASC-1 to ~90 nm in ASC-2. The average peak-to-valley separation distance (R_z) of the groups was ~0.5 nm in ASC-0.5 and ASC-1 and ~0.2 nm in ASC-2. Additionally, the scaffolds exhibited root mean square micro-roughness (Rq) values of 8.98, 41.1, 66.7, and 32.8 nm in the scanned area of ASF, ASC-0.5, ASC-1, and ASC-2, respectively. The MF-treated scaffolds displayed an increase in the roughness up to a concentration of 1% CNC compared to ASF. However, the decrease in the Rq value of ASC-2 might have resulted from concentration dependency of CNC alignment under MF treatment (De France et al., 2016).

The surface area in the scanned 2D planes was 25.1, 25.2, 25.6, and 25.6 μm^2 in ASF, ASC-0.5, ASC-1, and ASC-2, respectively. The increase in the roughness and surface area in the CNC-incorporated MF-treated scaffolds up to 2% CNC incorporation is expected to promote cell adhesion and proliferation (Ermis et al., 2018; Zhou, Li, et al., 2021).

Next, we analyzed the thickness of the wall in the MF-treated scaffolds to estimate the changes in strand organization. The average strand diameters of MF-treated ASF, ASC-0.5, ASC-1, and ASC-2 were measured to be 143, 150, 158, and 200 µm, respectively (Fig. S5). The gradual increment in the wall diameter of the scaffolds (ASC-0.5 to ASC-2) corresponds to a gradual increase in the assembly of CNCs as a response to the applied MF, thereby making a characteristic robust and aligned template for the surrounding Alg-SF interactions and controlled unidirectional ice crystal formation upon freezing. Fig. S6 shows the digital images of the scaffolds as fabricated.

3.2. *Interaction and crystallinity study*

The chemical interactions among the polymers were analyzed through FT-IR spectroscopy (Fig. S7). Sodium alginate is a polyelectrolyte macromolecule containing a large number of carboxyl groups. While some of the carboxyl groups remain non-ionized (–COOH), others are ionized in the form of $–COO^-Na^+$ (Aprilliza, 2017). Moreover, SF is a stereo-regular copolymer of alanine (30%) and glycine (44%) (Jung et al., 2021). Fig. S7 (A) shows the independent spectra of SF with the characteristic amide bands at 1642 cm^{-1} for amide I, 1514 cm^{-1} for amide II, and 1234 cm^{-1} for the amide III region, indicating the presence of both the α-helix and β-conformation in the polypeptide chain. Similarly, Alg shows the characteristic $–CH_2$ stretching at 2900 cm^{-1} and the –OH functional group at 3200–3400 cm^{-1}. The peaks at ~1596 cm^{-1} and 1422 cm^{-1} are attributed to the asymmetric and symmetric stretching of carboxylate $–COO^-$,

respectively. The intense peak at 1015 cm^{-1} corresponds to the C—H stretching. The low-intensity peaks at 1162 cm^{-1} are attributed to arabinosyl units, whereas the peak at 893 cm^{-1} shows glycosidic linkage. The FTIR spectra of the prepared CNCs show peaks at 3336 cm^{-1} (–OH region), 2900 cm^{-1} (C—H stretching vibration), 1430 cm^{-1} (symmetric bending), and 1320 cm^{-1} (CH_2 wagging at C6). The peaks at 1160, 1124, and 1065 cm^{-1} correspond to the sulfate ester bonds induced by the sulfuric acid hydrolysis during CNC preparation. For the ASF and ASC (0.5–2) scaffolds, the 1596 cm^{-1} peak of pure Alg shifted to 1500 cm^{-1}, whereas the 1422 cm^{-1} peak was retained as observed in Fig. S7 (B). The 1642 cm^{-1} peak of amide I was maintained; however, the 1514 cm^{-1} peak corresponding to amide II was not observed. Moreover, the C—H stretching at 1015 cm^{-1} appeared in the composite at ~1022 cm^{-1}. The obtained spectra show a possible interaction between the carboxylate of Alg and amide II of SF. No drastic change in the interaction was observed in the polymer matrix with the CNCs, indicating that the presence of CNCs causes templating of the polymer topology without altering the intrinsic properties.

Conformational changes in the prepared nanocomposite W/WO MF-treatment were determined by XRD analysis (Fig. 2 (A & B)). Without MF treatment (WO MF-treatment), a broad peak from ~7° to 13° (2θ = 14.54°) was observed for the ASC-2 samples; this peak was not prominent for ASF, ASC-0.5, and ASC-1, indicating the higher amorphous nature of ASC-2 due to increased concentration of CNCs. Moreover, a peak at 22.62° marked the characteristic crystalline peak of CNCs in the ASC scaffolds (ASC-0.5 to ASC-2). Upon MF-treatment, the crystallinity of the scaffolds significantly increased (by ~10%), as indicated by the increase in the peak intensity at 22.62° for the MF-treated ASC scaffolds. No changes in the spectral pattern at 22.62° were observed for ASF. The crystallinity was nearly doubled in the MF-treated samples (Fig. 2 (C)), indicated higher-order alignment in the overall polymer matrix owing to the magneto-responsiveness of the CNCs (Lagerwall et al., 2014; Sugiyama et al., 1992). However, there was no significant change in the overall structure of the nanocomposite.

To elucidate the molecular packaging arrangement of the CNCs in the polymer matrix, we performed SAXS analysis. The SAXS data provided a distinct 1D graph and 2D pattern of the fabricated scaffolds (Fig. 2 (D–G)). We observed a gradual shift in the scattering vector of the ASC scaffolds upon MF-treatment w.r.t. the untreated ASF and ASC-2 scaffolds (Fig. 2 (D)). CNC incorporation in the ASF matrix without MF-treatment has a minor effect on the scattering pattern, while the MF-treatment modifies the curves significantly. Furthermore, we observed a notable decrease in the inter particle distance 'd' in the MF-treated ASC scaffolds compared to the untreated samples by 10–15 nm (Fig. 2 (E)). These results are also reflected in the azimuthal intensity distribution pattern (Fig. 2 (F)). We observed a gradual narrowing of the azimuthal intensity profile from untreated ASF/ASC scaffold to MF-treated ASC scaffolds, indicating higher anisotropic particle orientation. Besides, the

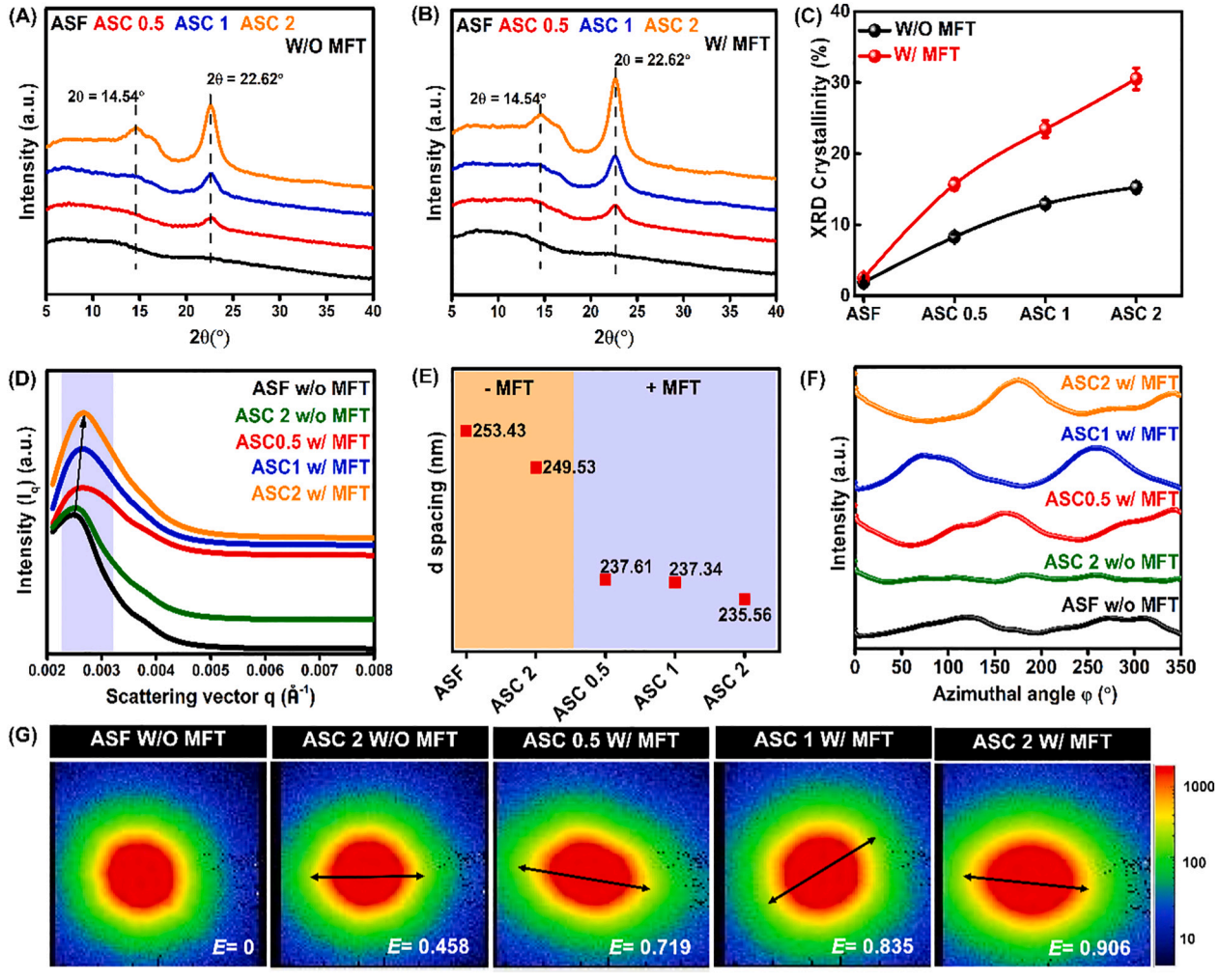

Fig. 2. Crystallinity and molecular anisotropy in the fabricated scaffolds. **(A–C)** XRD patterns of the samples **(A)** without, **(B)** with MF-treatment, **(C)** the corresponding crystallinity index; **(D–G)** SAXS pattern of the developed scaffold at measured region (q: scattering vector), **(D)** 1D graph of the SAXS pattern, **(E)** corresponding d spacing values, **(F)** azimuthal intensity profile, **(G)** 2D diffraction patterns. The black arrow indicates the orientation of diffraction circles with corresponding eccentricity (*E*) values.

2D diffraction patterns of the samples indicated a sharp increase in the eccentricity values confirming the anisotropy of the MF-treated scaffolds (Fig. 2 (G)). The highest eccentricity value was that of the MF-treated ASC-2 scaffold ($E = 0.906$), whereas the ASC-1 and ASC-0.5 scaffolds under MF-treatment showed an eccentricity of 0.835 and 0.719, respectively. Even lower eccentricity values were estimated for the ASF ($E = 0$) scaffold showing its isotropic nature. In comparison, ASC-2 ($E = 0.458$) scaffolds without MF stimulation showed slight anisotropy. To investigate the stability of the anisotropy in the MF-treated scaffolds on implantation, we examined the SAXS analysis of the ASC 0.5 scaffold upon hydration (Fig. S8). No change in the peak position for the MF-treated ASC-0.5 scaffold was observed after swelling for 5 days, indicating the retention of the scaffold integrity (Fig. S8 (A)). The eccentricity value of the MF-treated ASC 0.5 scaffold after 5 days' post hydration was observed to be reduced by ~0.2 (Fig. S8 (B)), indicating scaffold integrity.

3.3. Mechanical behavior

Mechanical strength of implants is vital in determining the effectiveness of tissue engineering scaffolds. Besides, anisotropy has been associated with an improved mechanical property of fabricated scaffolds (Sano et al., 2018). Fig. 3 (A, B) shows the stress-strain profile of the scaffolds w/wo MF-treatment. We have observed higher compressive stress in the ASC 0.5 scaffold w/wo MF-treatment among the other samples. Moreover, an increase of ~15 MPa was recorded for the ASC 0.5 scaffold after MF-treatment. Consequently, an increase in the Young's modulus was noted in the ASC 0.5 scaffold upon MF-treatment (~1.2 MPa) w.r.t. ASC 0.5 without MF-treatment (~0.6 MPa), indicating the robustness of the MF-treated scaffolds (Fig. 3 (C)). The Young's modulus observed for the MF-treated ASC 0.5 scaffold is in great consistent with the modulus of the human skin, which is 0.97–1.09 MPa (Annaidh et al., 2012). Synthetic scaffolds with high toughness are desirable for tissue formation (Negut et al., 2020). Fig. 3 (D) shows the measured toughness of the fabricated scaffolds W/WO MF-treatment. A ~2 MJ/m^3 increase in the toughness of the MF-treated ASC 0.5 scaffold was observed, which complements its use as a skin regeneration implant. We further examined the changes in the Young's modulus of the ASC 0.5 scaffold (W/WO MF-treatment) after 3 and 5 days of hydration to evaluate the retention of scaffold stiffness (Fig. S9). The differences in the mechanical properties of the MF-treated scaffolds are assumed to be affected by the orientation of the CNCs W/WO MF-treatment (Liu & Webster, 2010) which is highly affected by the viscoelastic property of the precursor gel. Hence, we observed the viscoelastic property of the precursor gel. We observed a shear-thinning behavior of the ASF/ASC (0.5–2) gels, indicating free movement of CNCs upon MF-stimulation (Fig. 3 (E & F)). At both 30 and 35 °C, the viscosity of the hydrogels decreased with an increase in shear rate. At a low shear rate (1 s^{-1}), the viscosity of the ASF, ASC-0.5, ASC-1, and ASC-2 hydrogels at 30 °C was 32,548.7, 104,281, 52,304.2, and 114,229 Pa·s, respectively. At 100 s^{-1},

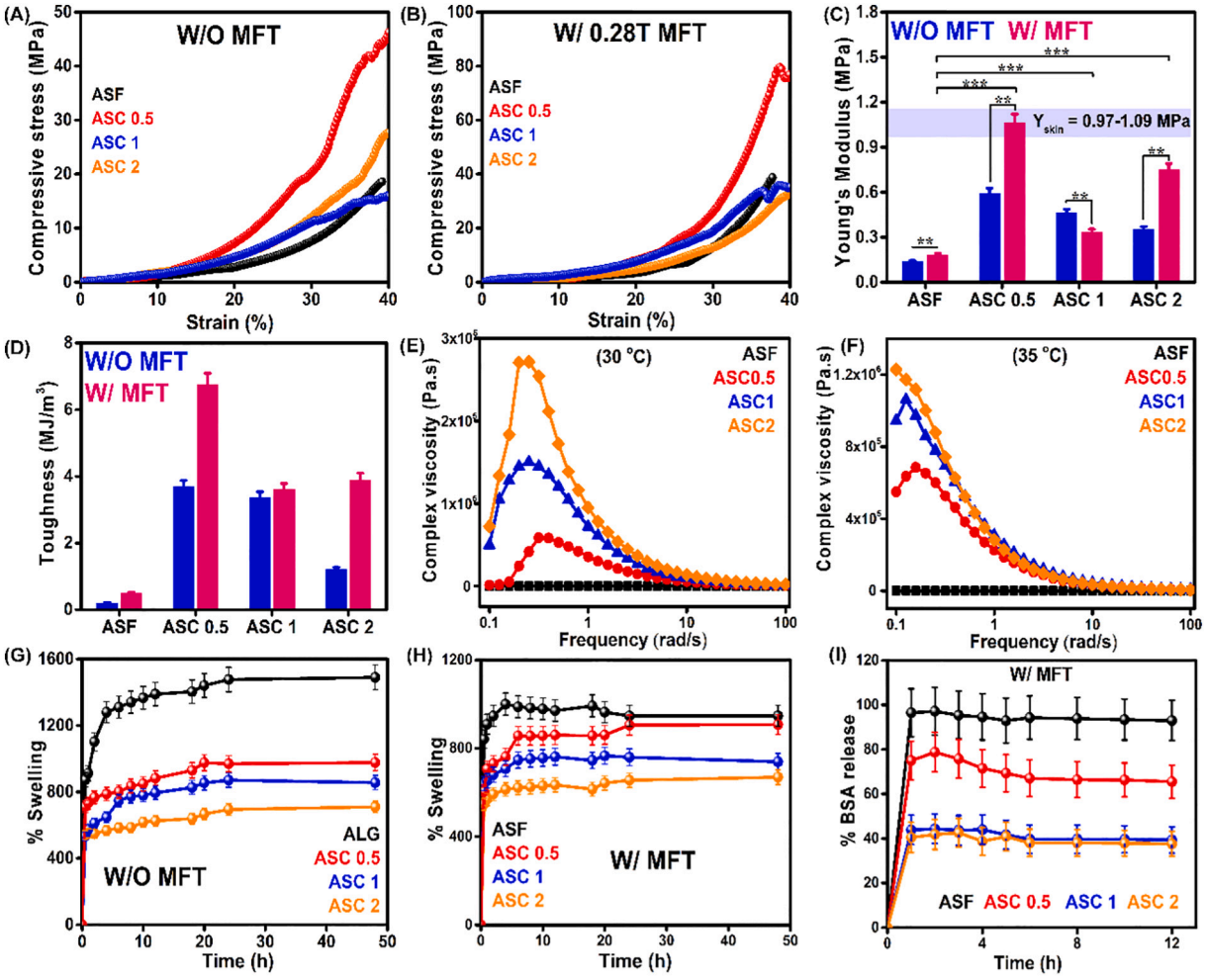

Fig. 3. Mechanical property assessment. Compressive stress **(A)** without, **(B)** with MF-treated scaffolds; Corresponding **(C)** Young's modulus and **(D)** Toughness of the scaffolds; **(E, F)** the change in the complex viscosity of the fabricated scaffolds with the angular frequency, **(G, H)** Percentage swelling at RT **(G)** without MF-treatment, **(H)** with MF-treatment; **(I)** BSA release profile at RT in the indicated time intervals.

the viscosity was found to increase to 64.3452, 191.686, 99.779, and 214.496 Pa·s, respectively. Similarly, at 35 °C, the viscosity of the hydrogels was 30,819.9, 101,231, 50,519.6, and 111,791 Pa·s at a low shear rate (1 s^{-1}); these increased to 59.5124, 183.137, 94.1411, and 205.217 Pa·s at 100 s^{-1} for ASF to ASC-2, respectively. The ASC hydrogels showed higher complex viscosity values than the ASF hydrogel throughout the scanned regions of ω under different temperature conditions. However, all the hydrogels showed higher complex viscosity values at 35 °C than at 30 °C.

The changes in the storage modulus (G′) and the loss modulus (G″) of the gels in the measured ω range are given in Fig. S10 (A & B). An enhanced G′ value was found throughout the measured ω regions for CNC-containing gels (ASC-0.5, ASC-1, and ASC-2) compared to that of ASF at both 30 and 35 °C. At 30 °C, the storage moduli of ASF, ASC-0.5, ASC-1, and ASC-2 at 0.1 rad/s were ~3163.43, 10,108.4, 5079.69, and 11,115.7 Pa, respectively, and the loss moduli were 766.08, 2562.58, 1246.6, and 2631.23 Pa. At 100 rad/s, the storage moduli of ASF, ASC-0.5, ASC-1, and ASC-2 were ~6314.29, 18,913.6, 9800.13, and 21,116.2 Pa, respectively, and the loss moduli were 1238.05, 3116.01, 1875.07, and 3766.64 Pa. The enhanced G′ values for the CNC-reinforced hydrogels were attributed to reduced motion of the polymer chains in the ASC hydrogels owing to the physical interactions between the CNCs and the polymer matrix. The G″ values were less than the G′ values for the CNC-containing hydrogels. However, the G″ values of the ASC hydrogels were higher than that of ASF at 30 °C (Fig. S10 (A)). A similar trend was observed for the rheological properties of the hydrogels at 35 °C; the G′ values of ASF, ASC-0.5, ASC-1, and ASC-2 at 0.1 rad/s were ~3000.03, 9834.66, 4916.23, and 10,904.6 Pa, respectively, and the G″ values were 706.002, 2399.5, 1163.17, and 2462.1 Pa. At 100 rad/s, the G′ values of ASF, ASC-0.5, ASC-1, and ASC-2 were ~5840.41, 18,071.5, 9250.99, and 20,215.7 Pa, respectively, and the G″ values were 1143.18, 2968.4, 1744.86, and 3530.8 Pa (Fig. S10 (B)). We anticipate that this behavior of the gels will be reflected in the scaffolds upon hydration for prolonged time interval.

3.4. Swelling and BSA release profile

The swelling efficiency of the fabricated scaffolds was analyzed at RT until equilibrium was attained to evaluate their hydration properties. As shown in Fig. 3 (G &H), ASF showed higher swelling efficiency than the CNC-incorporated scaffolds under both MF-treated or untreated samples. We observed a gradual decrease in the swelling behavior of the scaffolds with an increase in the CNC concentration (W/WO MFT). No significant difference was observed in the swelling behavior of the scaffolds W/WO MF-treatment. The ASF, ASC-0.5, ASC-1, and ASC-2 scaffolds were observed to swell by ~862.50%, 540%, 533.82%, and 364% within 30 min of immersion in PBS. Furthermore, a negligible swelling effect was observed in the scaffolds after 48 h of immersion, indicating the attainment of an equilibrium swelling state. The equilibrium swelling ratios of the scaffolds were ~1215%, 977%, 857%, and 712% for ASF to ASC-2, respectively. The inverse proportionality of CNC concentration to the scaffold swelling behavior can be attributed to the properties of CNCs as natural crosslinkers in the Alg-SF polymers. The CNCs in the polymer matrix promote a more compact and stable structure after crosslinking with the constituents of the scaffold (Sharma et al., 2015). A similar trend was observed in the swelling behavior of the MF-treatment treated scaffolds, indicating no drastic effect of scaffold alignment on swelling behavior of the samples.

Albumin is one of the vital proteins for wound healing (Zhou et al., 2018). Moreover, serum albumin reduction is associated with increased mortality in major skin injuries (Aguayo-Becerra et al., 2013). Hence, we investigated the *in vitro* BSA release behavior of the MF-treated scaffolds at RT as model protein (Fig. 3I). We anticipate a similar release profile of loaded proteins like growth factors from the prepared scaffolds under clinical conditions. The curve of BSA release from the scaffolds shows three distinct sections. An initial burst release within a few hours of soaking in PBS, a slow and steady release at the middle stage up to 20 h, and a gradual declining release slope up to 24 h. The percentage of BSA released from ASF, ASC-0.5, ASC-1, and ASC-2 after 2 h of immersion in PBS (pH 7.4) was noted to be ~97%, 78%, 44%, and 44%, respectively. The percentage of BSA release after 24 h of immersion was ~80%, 54%, 35%, and 31% from ASF to ASC-2, respectively. The release of BSA from all the scaffolds attained a maximum within a few hours of immersion under shaking conditions; however, the BSA release percentage decreased with an increase in the CNC concentration, consistent with the scaffold swelling properties. An addition of 0.5% (*w/v*) of CNCs in ASF resulted in a decrease in BSA release of ~19% within 2 h of soaking. A ~34% reduction in the BSA release was observed for both the ASC-1 and ASC-2 scaffolds. Additionally, the mineral adsorption property of any synthetic scaffold shows synergistic effect on wound healing (Abdal-hay et al., 2022; Li et al., 2020). Hence, mineral deposition on the fabricated MF-treated scaffolds was determined using the SEM/EDX micrographs revealing the Na, Cl, Ca, and P deposition after immersion in PBS for 48 h (Fig. S11). The Na/Cl ratios in the ASF and ASC scaffolds were 0.91, 0.71, 0.92, and 1.15. The deposition of Ca was highest in ASC-0.5 (2.72%), followed by ASC-2 (2.10%), ASF (0.66%), and ASC-1 (0.57%). Only ASC-0.5 was observed to have 2.09% P deposition. The effects of magnetic field stimulation on the physiochemical characteristics of the fabricated scaffolds has been summarized in (Table 1).

3.5. In vitro cytological evaluation

3.5.1. Biocompatibility assessment

The skin is a complex structure of distinct anatomical layers. Keratinocytes, dermal fibroblasts, and endothelial cells are the architectural constituents of the epidermis, dermis, and blood vessels, respectively (Yu et al., 2019). To establish guided wound healing of skin tissue, we studied the effect of the fabricated scaffolds on HDFs, HaCaT cells, and HUVECs in individual and co-culture systems. As the different aspects of ECM sensed by cells include biochemical cues (molecular composition and chemical moieties, including surface charges, hydrophilicity, and hydrophobicity), mechanical factors (elasticity and resilience of ECM), and topographical features (roughness, patterns, and porosity) (Chaudhuri et al., 2020), we began by investigating the cell viability, cell proliferation, cell morphology, cytoskeletal organization, and cell motility.

The proliferation of cells in the fabricated scaffolds over 5 days of culture was investigated. Cell viability was higher in all the scaffold-treated cells than in the negative control (cells seeded on TCPS) (Figs. 4 (A–C) and S12 (A)). HDFs on the 0.5% and 1% CNC-containing scaffolds were found to have the highest recorded viability until 5 days of treatment. A similar pattern was observed for the viability of HaCaT cells. In the case of HUVECs, an increase in cell viability was observed much earlier, at 3 days of treatment with ASC-0.5 and ASC-1, compared to that with ASF. Under co-culture conditions, an 80% and a 60% higher cell viability was observed in the presence of ASC-0.5 and ASC-1, respectively, compared to that of ASF, after 3 days of culture. Our results indicated that the anisotropic pores in ASC-0.5 and ASC-1 supported the maximum percentages of cell viability in all the cell culture conditions. The reduced cell viability in ASC-2 might have resulted from the low swelling nature of the scaffold. Based on our results, we hypothesized that ASC-0.5 would be a more reliable scaffold for further examination, with ASF as the control.

As HDFs drive a majority of the regulatory programs during wound healing (Abbasi et al., 2020), we also studied the biocompatibility of the ASF and ASC-0.5 scaffolds using the Live-Dead assay as a proof of concept. Fig. S12 (B) shows the microscopy images of HDFs cultured on ASF and ASC-0.5 for 1, 3, and 5 days. Both ASF and ASC-0.5 were found to profoundly support the viability of the HDFs. Moreover, a striking difference that proved topology-guided HDF proliferation was captured.

Table 1
Comparative study of the effect of magnetic field stimulation on the physiochemical characteristics of the fabricated scaffolds.

Parameter	W/O MFT				W/ MFT			
	ASF	ASC 0.5	ASC 1	ASC 2	ASF	ASC 0.5	ASC 1	ASC 2
Ultrastructure	Mostly non-homogenous	Flaky	Flaky	Weakly aligned	Mostly non-homogenous	Aligned	Highly aligned	Highly aligned
Orientation	Isotropic	Isotropic	Isotropic	Weakly anisotropic	Isotropic	Anisotropic	Highly anisotropic	Highly anisotropic
Crystallinity (%)	1.79 ± 0.09	8.24 ± 0.41	12.99 ± 0.64	15.18 ± 0.76	2.79 ± 0.12	15.62 ± 0.78	23.50 ± 1.17	30.51 ± 1.52
Mechanical properties	Y = 0.13 ± 0.006 T = 0.21 ± 0.01	Y = 0.59 ± 0.029 T = 3.69 ± 0.18	Y = 0.46 ± 0.006 T = 3.37 ± 0.16	Y = 0.35 ± 0.017 T = 1.21 ± 0.06	Y = 0.18 ± 0.009 T = 0.50 ± 0.02	Y = 1.06 ± 0.053 T = 6.75 ± 0.33	Y = 0.33 ± 0.016 T = 3.60 ± 0.18	Y = 0.75 ± 0.03 T = 3.90 ± 0.19

Y, Young's modulus; T, Toughness.

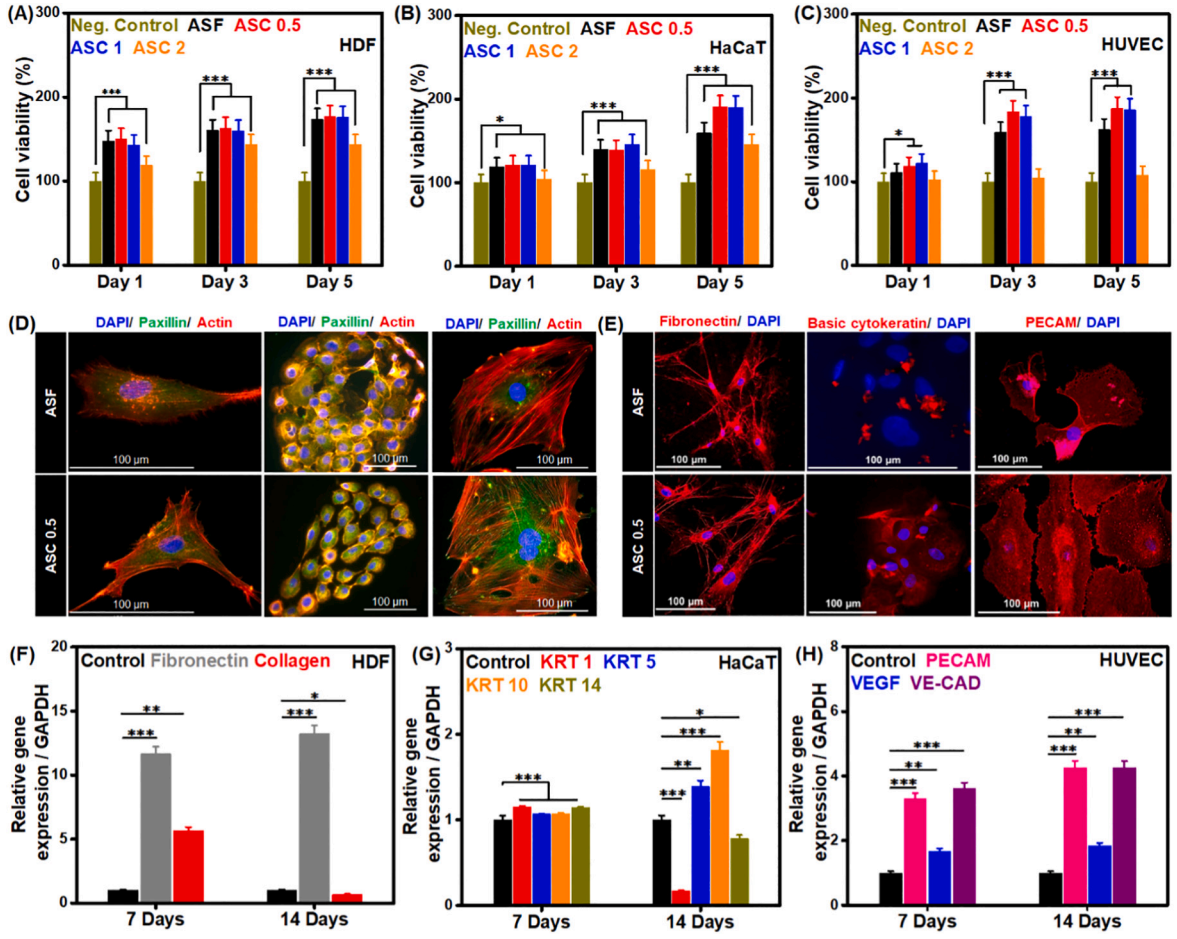

Fig. 4. *In vitro* biocompatibility assessment of the fabricated scaffolds. **(A–C)** The cell viability assessment of **(A)** HDF, **(B)** HaCaT, **(C)** HUVEC, **(D)** Immunofluorescence staining of HDF, HaCaT, and HUVEC in the presence of MF-treated ASF and ASC-0.5 scaffolds showing the focal adhesion points (Paxillin; green), cytoskeleton (F-actin; red), and nucleus (DAPI; blue) after 3 days of culture (HDF, left; HaCaT, middle; and HUVEC, right). **(E)** Representative fluorescence microscopy images of fibronectin, basic cytokeratin, and PECAM in HDF, HaCaT, and HUVEC, respectively (HDF, left; HaCaT, middle; and HUVEC, right); **(F–H)** Real-time polymerase chain reaction (qRT-PCR) analysis of marker genes in the **(F)** HDF, **(G)** HaCaT, and **(H)** HUVEC after indicated time intervals. Data are mean ± SD of triplicated experiments, statistical significance at $*p < 0.05$, $**p < 0.01$, and $***p < 0.001$. Scale bar: 100 μm. (For interpretation of the references to colour in this figure legend, the reader is referred to the web version of this article.)

3.5.2. Cell cycle, cell morphology, and cell migration assessment

We analyzed the cell cycle progression of HDFs, HaCaT cells, and HUVECs cultured individually in the presence of ASF and ASC-0.5 for 24 h to confirm their proliferation stages (Fig. S13 (A)). We found an ~7% increase in DNA content in the G0/G1 phase of HDFs cultured on ASC-0.5, with respect to that on ASF. However, an ~6% decrease in the DNA content of the HDFs cultured on ASC-0.5, compared to that on ASF, at the G2/M phase was recorded. This result indicates that the aligned walls in ASC-0.5 support slower proliferation of HDFs; this is expected to favor the anti-fibrotic effect during wound healing (Masub et al., 2021). No significant difference in the cell proliferation stages of HaCaT cells was noticed, whereas a 2% increase was observed in the G2/M phase of HUVECs cultured on ASC-0.5, w.r.t. that on ASF. Our results indicated that the fabricated scaffolds had a nearly similar effect on the cultured cells after 24 h.

Next, we checked the cell morphology of the co-cultured cells using

SEM microscopy after 3 days of culture, as shown in Fig. S13 (B). Co-cultured cells seeded on the ASF and ASC-0.5 scaffolds demonstrated distinct morphological features and surface adhesion affinities. We observed higher cell numbers within the scanned area adhering to the ASC-0.5 scaffold than that on the control scaffold. Furthermore, we observed a more flattened cell structure with a large number of filopodial protrusions on ASC-0.5 and rod-shaped cells with smaller filopodial outgrowth on the control scaffold. The number of filopodia per cell was also higher in the ASC-0.5 scaffold, indicating a higher affinity of the cells toward the ASC-0.5 scaffold. Figs. S13 (C) and S14 (A–C) compare the cell aspect ratio on the scaffolds. HDFs and HaCaT cells grown on ASC-0.5 showed more horizontal expansion, whereas no difference was observed in the aspect ratio of the HUVECs. Higher aspect ratio cells are expected to enhance contact guidance-mediated wound healing by sensing the anisotropy of the implanted scaffolds (Casale et al., 2021; Ge et al., 2020; Thrivikraman et al., 2021).

Furthermore, we checked the migration of the co-cultured cells in the presence of the fabricated scaffolds W/WO loaded growth factor(s). As shown in Fig. S13 (D & E), migration of the cells in the presence of ASF and ASC-0.5 was nearly similar after 12 h of culture, although a 20% rise in the number of cells migrating in the presence of ASC-0.5 was obvious after 24 h of treatment. The ASC-0.5 scaffold was further supplemented with 500 nM growth factors, including VEGF and EGF, to study the synergistic effect of growth factors released from the scaffold on cell migration. We observed that the cell migration doubled upon VEGF supplementation by the end of 24 h, and a threefold increase in cell migration was observed in the ASC-0.5 scaffold supplemented with VEGF/EGF. Hence, we assume that the MF-treated ASC-0.5 scaffold has more potential to stimulate rapid cell migration, which increases upon the addition of growth factors.

3.5.3. Cytoskeletal arrangement

Next, we investigated the cytoskeletal arrangement of the cultured cells in the presence of the fabricated scaffolds. Fig. 4 (D) shows the immunofluorescence images of the cells expressing actin and paxillin among HDFs, HaCaT cells, and HUVECs after 3 days of culturing on the ASF and the ASC-0.5 scaffolds. A significant increase in the number of focal adhesion points in cells cultured on the MF-treated scaffold was evident for HDFs and HUVECs. Unlike the shrunken morphology of the ASF-cultured HDFs and HUVECs, the cells cultured on ASC-0.5 were fully spread out on the ECM through abundant focal adhesion points. When comparing the morphology of the individual HaCaT keratinocytes on the porous and aligned scaffolds, we observed a well-spread morphology on the MF-treated scaffold. In contrast, more round cells were observed on the control scaffold. This morphological difference might have originated from the difference in pore dimension of the control and aligned scaffolds, since HaCaT cells have been reported to adapt their morphology depending on the surrounding ECM (Kong et al., 2017).

3.5.4. Wound healing marker expression

As wound healing is a complex process involving the expression of crucial proteins (Yussof et al., 2012), we studied the expression of some selected marker genes and proteins. To evaluate the wound healing efficiency of the ASC-0.5 scaffold, we checked the protein expression profile of selected marker proteins, including fibronectin (Johnson et al., 2017), basic cytokeratin (Tang et al., 2021), and PECAM (Bruggisser et al., 2020) in HDFs, HaCaT cells, and HUVECs, respectively, after 14 days of culturing. As shown in Fig. 4E, fibronectin was expressed throughout the cytosol and filopodial projections in HDFs cultured with ASF and ASC-0.5. Higher expression of fibronectin has long been associated with wound healing. It is one of the major adhesive proteins that promote ECM formation and skin epithelialization. Fibronectin is widely known to interact with different types of cells and cytokines (Lenselink, 2015).

Moreover, a fibronectin-coated matrix has also been shown to accelerate skin wound healing in mouse models (Jara et al., 2020). Hence, the higher expression of fibronectin in ASC-0.5-cultured HDFs is consistent with previously established reports. A striking difference was observed in the expression of basic cytokeratin in HaCaT cells. Cytokeratin was expressed around the nucleus of the cells cultured with ASF. However, it was expressed throughout the cytosol of HaCaT cells cultured with ASC-0.5. The higher level of expression of basic cytokeratin in the cells cultured on ASC-0.5 indicates the active metabolic stages in the cells (Bragulla & Homberger, 2009). Similarly, PECAM was expressed throughout the cytosol of HUVECs cultured with both ASF and ASC-0.5. However, the expression was more centered near the nucleus in the ASF-cultured cells. A more homogenous expression of PECAM was observed in the cells cultured with ASC-0.5. PECAM is widely expressed in all vascular compartment cells and promotes angiogenesis (Woodfin et al., 2007). Hence, our result indicates that ASC-0.5 must promote rapid angiogenesis.

Next, we analyzed the gene expression of common epithelization markers in HDFs (fibronectin and collagen) and HaCaT cells (KRT1/10, KRT5/14) and angiogenic markers in HUVECs (PECAM, VEGF, and VE-CAD) involved in the wound healing process. As shown in Fig. 4F, a sharp increase (~10 fold) in the expression of the matrix protein fibronectin was observed after 7 days of culture of the HDFs, which expressed marginally more (~11%) up to 14 days of culture with the MF-treated scaffold. However, a decrease in collagen expression was noticed after 14 days of HDF culture, probably due to *in vitro* cell aging. Collagen is an abundant protein that widely participates in wound healing (Ramanathan et al., 2020; Thapa et al., 2020). We also examined the expression levels of basic keratins, including KRT1, KRT5, KRT10, and KRT14, in HaCaT cells. An increase in the expression of KRT1, KRT5, KRT10, and KRT14 was observed in the presence of ASC-0.5 after 7 days of culture. However, a decrease in the expression of KRT1 and KRT14 was observed after 14 days of culture (Fig. 4G). Differential expression of KRT genes might indicate the transition between early and late stages of keratinocyte differentiation (Zhang et al., 2021). We observed an increase in the expression of PECAM, by 2.5- and 3-fold, after 7 and 14 days, respectively, in HUVECs cultured with ASC-0.5. A 1-fold rise in VEGF expression was observed after 7 and 14 days of culture. The expression of VE-CAD in the presence of the ASC-0.5 scaffold up to 14 days of cell culture increased 3-fold with respect to that in ASF-treated cells (Fig. 4H). The higher expression of VE-CAD is expected to result in higher cell-cell adhesion (Paatero et al., 2018). The expression of VEGF and PECAM is highly similar to previously reported results of scaffold topology-induced angiogenesis in HUVECs (Xiao et al., 2015). Next, we checked the secretome of the co-cultured cells in the presence of ASF and ASC-0.5 to detect released growth factors Fig. S15 (A & C). We observed differential secretion of several growth factors, among which a few indicated a relevant role in wound healing. A more than 1-fold change was observed in the secretion of GM-CSF, HB-EGF, and PDGF-AA in the presence of ASC-0.5. GM-CSF has been reported to promote wound healing by inducing keratinocyte proliferation and epithelial cell migration (Rho et al., 2015). In comparison, HB-EGF has intriguingly been associated with keratinocyte migration-mediated wound remodeling (Peng et al., 2017). PDGF-AA is a critical molecule that stimulates fibroblast chemotaxis, proliferation, and gene expression (Pierce et al., 1991).

Additionally, a 2-fold increase in the secretion of EGFR, IGFBP3, IGFBP4, and IGFBP6 was observed. In contrast, a 3-fold increase in the secretion of VEGF-A was observed. Our results indicate that ASC-0.5 is a highly efficient wound healing scaffold. We studied multi-pathway phosphorylation events to examine the changes in the signaling pathway associated with HDFs, as they are critical components in the wound healing process (Fig. S15 (B & D)). A ~3-fold increase in the phosphorylation of Akt pS473 was detected, whereas a ~1-fold increase in the phosphorylation of GSK3A (pS21), JNK (pT183), MKK3, mTOR, and p38 was observed. Based on our results, we anticipate that the ASC-0.5 topology might predominantly trigger Akt phosphorylation at S473,

resulting in topology-guided dynamic cell physiology (Xing et al., 2015).

We conducted a bioinformatics string analysis to determine the possible interactions under the co-culture condition of the cells cultured with ASC-0.5, as shown in Fig. S15 (E–G). Five distinct categories were identified, including proteins involved in the structural and protective function in the epithelium (HRT1, HRT5, HRT10, and HRT14); factors associated with endothelial cell biology (GPER1, CD5, PECAM1), skin remodeling, and immunity (PDGFA, EGFR, VEGF-A, CSF2); proteins involved with the ECM component (Col1A1, Fibronectin 1); and growth factors associated with cell proliferation and migration (IGFBP3, IGFBP4, and IGFBP6). Moreover, through a protein-protein interaction study, we observed that over 30 genes involved in skin development, epithelialization, wound healing, and angiogenesis were the leading players of the healing process. Additionally, over 10 genes were found to apply in the growth factor and protein-binding activity (Fig. S15 (F & G)).

3.6. *In vivo* skin tissue regeneration

Based on the *in vitro* results demonstrating the potential benefits of ASC-0.5 in skin cell proliferation, migration, and overall cellular functions, we further evaluated this aspect in a subcutaneous skin wound model (10 mm) using male ICR rats (Fig. 5). Topology has been previously demonstrated to regulate cell behavior in numerous studies (Chen, Yu, et al., 2022; Wang et al., 2021). Fig. 5 (A) shows the schematics of the scaffold treatment period and the procedures applied for scaffold implantation. Fig. 5 (B) shows the images of the wounds on days 7 and 14. The wound closure rate was significantly higher (over 50%) in the ASC 0.5-treated rat within 7 days of treatment. The wound healing area differed in the ASF- and ASC-0.5-treated groups even after 14 days of wounding. We observed the formation of new skin in the ASC-0.5-treated scaffold, unlike in the blank and the ASF counterpart. However, wound scars persisted in all the experimental groups (Fig. 5C).

Histological analysis of the wound-tissue sections was performed after 14 days of scaffold implantation to observe neoepithelialization and new-tissue formation using H & E staining (Fig. 6A). Our results indicate that the damaged epidermis was nearly healed in all the groups; however, a distinct neoepidermal layer of regular thickness was observed in the scaffold-treated groups. Wounds implanted with ASF and ASC-0.5 had comparable thickness of the neoepidermis (Fig. 6C). Additionally, complete formation of the keratinized layer in the ASC-0.5-implanted tissue suggests completion of wound maturation. H & E staining also revealed the construction of new tissue at 14-day intervals. A dense accumulation of fibroblasts increased the number of blood vessels in the dermis, and the skin structures were restored more rapidly in the ASC-0.5-treated group than in the blank and ASF-implanted counterpart (Fig. 6D). To further investigate the efficiency of the ASC scaffold in wound healing, we examined collagen deposition after 14 days of treatment. Masson staining showed an increase in the formation of collagen fibers in the ASC scaffold-treated wounds compared to that in the blank and ASF groups. Moreover, the collagen deposition was accompanied by cutaneous and subcutaneous appendages in the ASF- and ASC-treated groups, unlike in the blank (Fig. 6B). These results confirmed that the maturation and remodeling stage was nearly achieved.

4. Conclusion

In this work, the effect of a low-strength magnetic field on the topology of CNC-based nanocomposites was studied. Our results showed that an 8 h exposure of the fabricated nanocomposite to the magnetic field had a significant impact on the alignment of the overall polymer matrix. Higher concentrations of CNCs in the Alg-SF polymer matrix resulted in an increase in the molecular packaging and parallel alignment and improved the physicochemical and mechanical properties. The enhanced cellular activity was confirmed using the physiological responses of cells cultured on the ASC-0.5 scaffold. ASC-0.5 supported cell viability, proliferation, and migration of HDFs, HaCaT cells, and

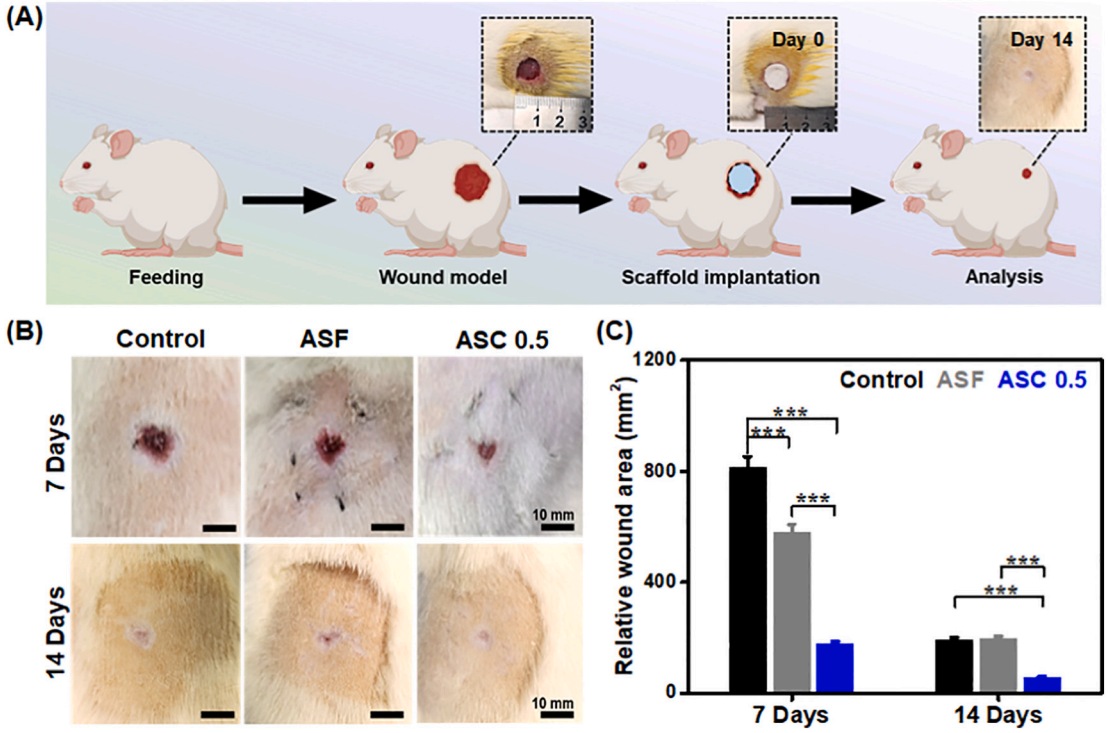

Fig. 5. *In vivo* assessment of the efficiency of the fabricated scaffolds. **(A)** Schematic of the *in vivo* assay procedure and the time frame of histological tissue staining; **(B)** Digital images of the wound closure rate after 7 and 14 days of scaffold implantation; **(C)** Quantification of the wound closure area after indicated time intervals. Scale bar: 10 mm.

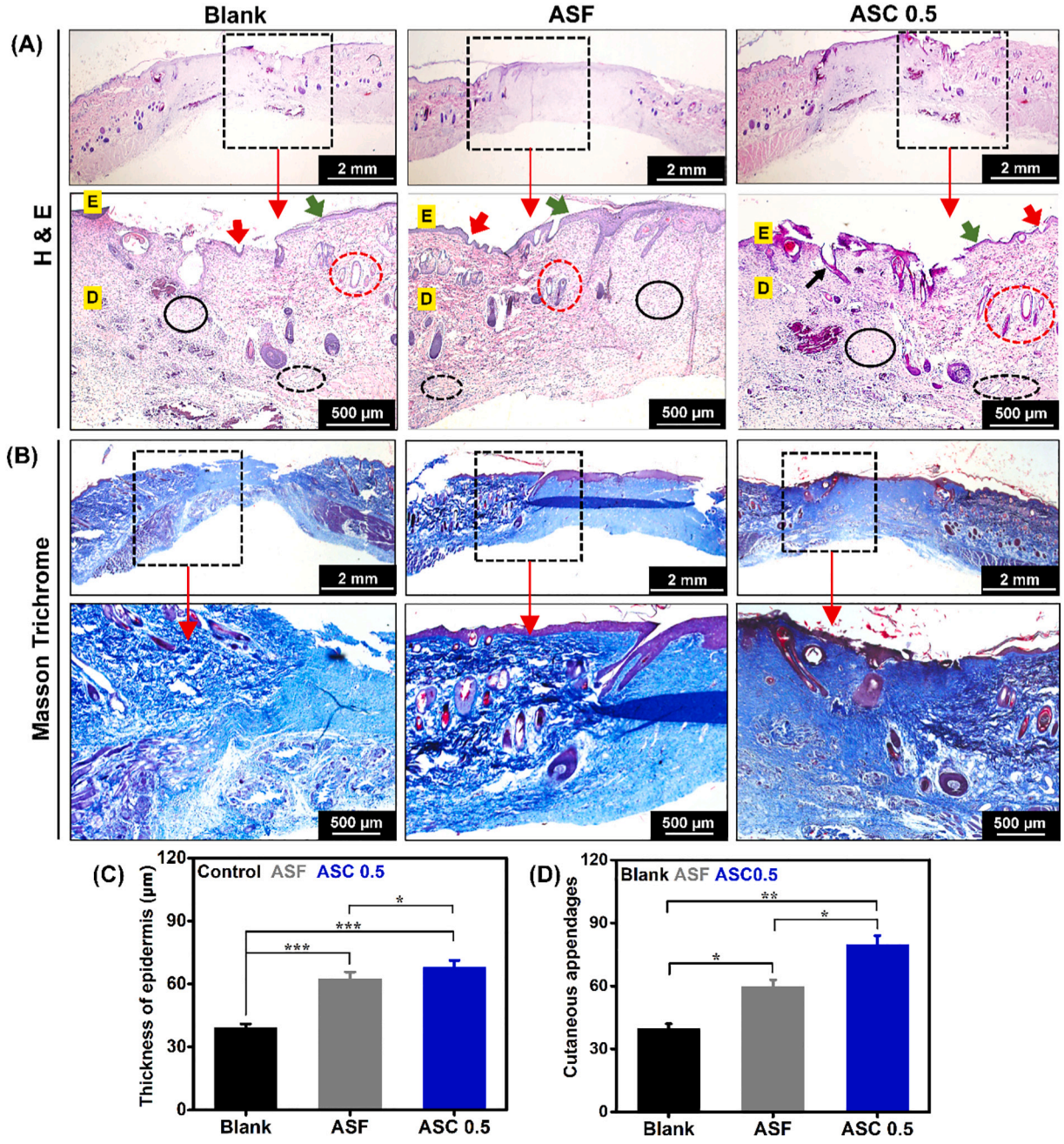

Fig. 6. *In vivo* assessment of the efficiency of the fabricated scaffolds. **(A)** H&E staining of the newly formed tissue after 14 days of treatment, **(B)** Masson trichrome staining for the assessment of collagen deposition 14 days' post-surgery. **(C)** Quantification of the thickness of the newly formed epidermis after 14 days of scaffold implantation; **(D)** Quantitative analysis of the number of cutaneous appendages formed after 14 days of treatment, Scale bar: 500 μm and 2 mm.

HUVECs in individual and co-culture systems to the maximum potential among the fabricated scaffolds. Differential expression of wound healing marker genes, proteins, and growth factors further confirmed the role of topology in wound healing. The wound healing ability of the aligned scaffold was also evaluated in a rat model, further demonstrating its bioactivity. Hence, the use of CNCs under a low-strength magnetic field could significantly support the fabrication of an aligned polymeric scaffold, paving the way for the use of CNCs as an excellent MF-responsive nanomaterial for tissue engineering applications.

CRediT authorship contribution statement

Keya Ganguly: Conceptualization, Methodology, Investigation, Visualization, Data curation, Formal analysis, Writing – original draft, Writing – review & editing. **Hexiu Jin:** Investigation, Data curation. **Sayan Deb Dutta:** Conceptualization, Investigation, Formal analysis. **Dinesh K. Patel:** Methodology, Formal analysis. **Tejal V. Patil:** Investigation, Formal analysis. **Ki-Taek Lim:** Supervision, Funding acquisition, Project administration, Writing – review & editing.

Declaration of competing interest

The authors declare no competing financial interest.

Acknowledgments

The authors would like to thank the Korea Basic Science Institute (KBSI), Chuncheon center, Republic of Korea, and Sungkyunkwan

University, Republic of Korea, for providing TEM image and rheological analysis respectively. This work was supported by the “Basic Science Research Program” through the “National Research Foundation of Korea” (NRF-2018R1A6A1A03025582 and 2019R1D1A3A03103828), Republic of Korea.

Appendix A. Supplementary data

Supplementary data to this article can be found online at https://doi.org/10.1016/j.carbpol.2022.119321.

References

Abbasi, S., Sinha, S., Labit, E., Rosin, N. L., Yoon, G., Rahmani, W., Jaffer, A., Sharma, N., Hagner, A., & Shah, P. (2020). Distinct regulatory programs control the latent regenerative potential of dermal fibroblasts during wound healing. *Cell Stem Cell, 27* (396–412), Article e396.

Abdal-hay, A., Sheikh, F. A., Gómez-Cerezo, N., Alneairi, A., Luqman, M., Pant, H. R., & Ivanovski, S. (2022). A review of protein adsorption and bioactivity characteristics of poly ε-caprolactone scaffolds in regenerative medicine. *European Polymer Journal, 162*, Article 110892.

Abitbol, T., & Cranston, E. D. (2014). Directed assembly of oriented cellulose nanocrystal films. In *Handbook of green materials: 3 self-and direct-assembling of bionanomaterials* (pp. 79–103). World Scientific.

Aguayo-Becerra, O. A., Torres-Garibay, C., Macías-Amezcua, M. D., Fuentes-Orozco, C., Chávez-Tostado, M.d. G., Andalón-Dueñas, E., Partida, A. E., Álvarez-Villaseñor, A. D. S., Cortés-Flores, A. O., & González-Ojeda, A. (2013). Serum albumin level as a risk factor for mortality in burn patients. *Clinics, 68*, 940–945.

Annaidh, A. N., Bruyère, K., Destrade, M., Gilchrist, M. D., & Otténio, M. (2012). Characterization of the anisotropic mechanical properties of excised human skin. *Journal of the Mechanical Behavior of Biomedical Materials, 5*, 139–148.

Aprilliza, M. (2017). Characterization and properties of sodium alginate from brown algae used as an ecofriendly superabsorbent. In *Paper presented at: IOP conference series: materials science and engineering*. IOP Publishing.

Babaei-Ghazvini, A., Cudmore, B., Dunlop, M. J., Acharya, B., Bissessur, R., Ahmed, M., & Whelan, W. M. (2020). Effect of magnetic field alignment of cellulose nanocrystals in starch nanocomposites: Physicochemical and mechanical properties. *Carbohydrate Polymers, 247*, Article 116688.

Bragulla, H. H., & Homberger, D. G. (2009). Structure and functions of keratin proteins in simple, stratified, keratinized and cornified epithelia. *Journal of Anatomy, 214*, 516–559.

Bruggisser, J., Tarek, B., Wyder, M., Müller, P., von Ballmoos, C., Witz, G., Enzmann, G., Deutsch, U., Engelhardt, B., & Posthaus, H. (2020). CD31 (PECAM-1) serves as the endothelial cell-specific receptor of clostridium perfringens β-toxin. *Cell Host & Microbe, 28*(69–78), Article e66.

Builles, N., Janin-Manificat, H., Malbouyres, M., Justin, V., Rovère, M.-R., Pellegrini, G., Torbet, J., Hulmes, D. J., Burillon, C., & Damour, O. (2010). Use of magnetically oriented orthogonal collagen scaffolds for hemi-corneal reconstruction and regeneration. *Biomaterials, 31*, 8313–8322.

Casale, C., Imparato, G., Mazio, C., Netti, P. A., & Urciuolo, F. (2021). Geometrical confinement controls cell, ECM and vascular network alignment during the morphogenesis of 3D bioengineered human connective tissues. *Acta Biomaterialia, 131*, 341–354.

Chaudhuri, O., Cooper-White, J., Janmey, P. A., Mooney, D. J., & Shenoy, V. B. (2020). Effects of extracellular matrix viscoelasticity on cellular behaviour. *Nature, 584*, 535–546.

Chen, L., Yu, Q., Jia, Y., Xu, M., Wang, Y., Wang, J., Wen, T., & Wang, L. (2022a). Micro-and-nanometer topological gradient of block copolymer fibrous scaffolds towards region-specific cell regulation. *Journal of Colloid and Interface Science, 606*, 248–260.

Chen, Q., Zhang, X., Chen, K., Wu, X., Zong, T., Feng, C., & Zhang, D. (2022b). Anisotropic hydrogels with enhanced mechanical and tribological performance by magnetically oriented nanohybrids. *Chemical Engineering Journal, 430*, Article 133036.

Chen, W., Zhang, Y., Kumari, J., Engelkamp, H., & Kouwer, P. H. (2021). Magnetic stiffening in 3D cell culture matrices. *Nano Letters, 21*, 6740–6747.

De France, K. J., Yager, K. G., Hoare, T., & Cranston, E. D. (2016). Cooperative ordering and kinetics of cellulose nanocrystal alignment in a magnetic field. *Langmuir, 32*, 7564–7571.

Dhar, P., Kumar, A., & Katiyar, V. (2016). Magnetic cellulose nanocrystal based anisotropic polylactic acid nanocomposite films: Influence on electrical, magnetic, thermal, and mechanical properties. *ACS Applied Materials & Interfaces, 8*, 18393–18409.

Ermis, M., Antmen, E., & Hasirci, V. (2018). Micro and nanofabrication methods to control cell-substrate interactions and cell behavior: A review from the tissue engineering perspective. *Bioactive Materials, 3*, 355–369.

Farahani, M., & Shafiee, A. (2021). Wound healing: From passive to smart dressings. *Advanced Healthcare Materials, 2100477*.

Farokhi, M., Mottaghitalab, F., Fatahi, Y., Khademhosseini, A., & Kaplan, D. L. (2018). Overview of silk fibroin use in wound dressings. *Trends in Biotechnology, 36*, 907–922.

Farzaneh, S., Hosseinzadeh, S., Samanipour, R., Hatamie, S., Ranjbari, J., & Khojasteh, A. (2021). Fabrication and characterization of cobalt ferrite magnetic hydrogel combined with static magnetic field as a potential bio-composite for bone tissue engineering. *Journal of Drug Delivery Science and Technology, 102525*.

Frka-Petesic, B., Guidetti, G., Kamita, G., & Vignolini, S. (2017). *Research data supporting" Controlling the Photonic Properties of Cholesteric Cellulose Nanocrystal Films with Magnets"*.

Ge, L., Yang, L., Bron, R., Burgess, J. K., & van Rijn, P. (2020). Topography-mediated fibroblast cell migration is influenced by direction, wavelength, and amplitude. *ACS Applied Bio Materials, 3*, 2104–2116.

Gelmi, A., & Schutt, C. E. (2021). Stimuli-responsive biomaterials: Scaffolds for stem cell control. *Advanced Healthcare Materials, 10*, 2001125.

Han, H., Chen, W., Yang, J., Liang, X., Wang, Y., Li, Q., Yang, Y., & Li, K. (2018). Inhibition of cell proliferation and migration through nucleobase-modified polyamidoamine-mediated p53 delivery. *International Journal of Nanomedicine, 13*, 1297.

Han, J., Zhou, C., Wu, Y., Liu, F., & Wu, Q. (2013). Self-assembling behavior of cellulose nanoparticles during freeze-drying: Effect of suspension concentration, particle size, crystal structure, and surface charge. *Biomacromolecules, 14*, 1529–1540.

Hao, S., Zhang, Y., Meng, J., Liu, J., Wen, T., Gu, N., & Xu, H. (2018). Integration of a superparamagnetic scaffold and magnetic field to enhance the wound-healing phenotype of fibroblasts. *ACS Applied Materials & Interfaces, 10*, 22913–22923.

Huang, Z., He, Y., Chang, X., Liu, J., Yu, L., Wu, Y., Li, Y., Tian, J., Kang, L., & Wu, D. (2020). A magnetic iron oxide/polydopamine coating can improve osteogenesis of 3D-printed porous titanium scaffolds with a static magnetic field by upregulating the TGFβ-Smads pathway. *Advanced Healthcare Materials, 9*, 2000318.

Irons, T. J., David, G., & Teale, A. M. (2021). Optimizing molecular geometries in strong magnetic fields. *Journal of Chemical Theory and Computation, 17*, 2166–2185.

Jara, C. P., Wang, O., do Prado, T. P., Ismail, A., Fabian, F. M., Li, H., Velloso, L. A., Carlson, M. A., Burgess, W., & Lei, Y. (2020). Novel fibrin-fibronectin matrix accelerates mice skin wound healing. *Bioactive Materials, 5*, 949–962.

Johnson, M. B., Pang, B., Gardner, D. J., Niknam-Benia, S., Soundarajan, V., Bramos, A., Perrault, D. P., Banks, K., Lee, G. K., & Baker, R. Y. (2017). Topical fibronectin improves wound healing of irradiated skin. *Scientific Reports, 7*, 1–10.

Jung, D., Lee, J., Park, T. Y., Yang, Y. J., & Cha, H. J. (2021). Diverse silk and silk-like proteins derived from terrestrial and marine organisms and their applications. *Acta Biomaterialia, 136*, 56–71.

Kong, D., Nguyen, K., Megone, W., Peng, L., & Gautrot, J. (2017). The culture of HaCaT cells on liquid substrates is mediated by a mechanically strong liquid–liquid interface. *Faraday Discussions, 204*, 367–381.

Kus, K. J., & Ruiz, E. S. (2020). Wound dressings–A practical review. *Current Dermatology Reports*, 1–11.

Lagerwall, J. P., Schütz, C., Salajkova, M., Noh, J., Park, J. H., Scalia, G., & Bergström, L. (2014). Cellulose nanocrystal-based materials: From liquid crystal self-assembly and glass formation to multifunctional thin films. *NPG Asia Materials, 6*, Article e80.

Lavrador, P., Esteves, M. R., Gaspar, V. M., & Mano, J. F. (2021). Stimuli-responsive nanocomposite hydrogels for biomedical applications. *Advanced Functional Materials, 31*, 2005941.

Lenselink, E. A. (2015). Role of fibronectin in normal wound healing. *International Wound Journal, 12*, 313–316.

Li, Y., Xu, T., Tu, Z., Dai, W., Xue, Y., Tang, C., Gao, W., Mao, C., Lei, B., & Lin, C. (2020). Bioactive antibacterial silica-based nanocomposites hydrogel scaffolds with high angiogenesis for promoting diabetic wound healing and skin repair. *Theranostics, 10*, 4929.

Liu, H., & Webster, T. J. (2010). Mechanical properties of dispersed ceramic nanoparticles in polymer composites for orthopedic applications. *International Journal of Nanomedicine, 5*, 299.

Liu, T.-L., Miao, J.-C., Sheng, W.-H., Xie, Y.-F., Huang, Q., Shan, Y.-B., & Yang, J.-C. (2010). Cytocompatibility of regenerated silk fibroin film: A medical biomaterial applicable to wound healing. *Journal of Zhejiang University Science B, 11*, 10–16.

Margolis, G., Polyak, B., & Cohen, S. (2018). Magnetic induction of multiscale anisotropy in macroporous alginate scaffolds. *Nano Letters, 18*, 7314–7322.

Martínez-Mora, C., Mrowiec, A., García-Vizcaíno, E. M., Alcaraz, A., Cenis, J. L., & Nicolás, F. J. (2012). *Fibroin and sericin from Bombyx mori silk stimulate cell migration through upregulation and phosphorylation of c-Jun*.

Masub, N., Austin, E., Huang, A., & Jagdeo, J. (2021). High-fluence light emitting diode-red light inhibits cell cycle progression in human dermal fibroblasts. *Journal of Biophotonics, 14*, Article e202000359.

Naomi, R., Ratanavaraporn, J., & Fauzi, M. B. (2020). Comprehensive review of hybrid collagen and silk fibroin for cutaneous wound healing. *Materials, 13*, 3097.

Negut, I., Dorcioman, G., & Grumezescu, V. (2020). Scaffolds for wound healing applications. *Polymers, 12*, 2010.

Nour, S., Imani, R., Chaudhry, G. R., & Sharifi, A. M. (2021). Skin wound healing assisted by angiogenic targeted tissue engineering: A comprehensive review of bioengineered approaches. *Journal of Biomedical Materials Research Part A, 109*, 453–478.

Onbas, R., & Arslan Yildiz, A. (2021). Fabrication of tunable 3D cellular structures in high volume using magnetic levitation guided assembly. *ACS Applied Bio Materials, 4*, 1794–1802.

Paatero, I., Sauteur, L., Lee, M., Lagendijk, A. K., Heutschi, D., Wiesner, C., Guzmán, C., Bieli, D., Hogan, B. M., & Affolter, M. (2018). Junction-based lamellipodia drive endothelial cell rearrangements in vivo via a VE-cadherin-F-actin based oscillatory cell-cell interaction. *Nature Communications, 9*, 1–13.

Park, K.-J., Shin, E.-J., Kim, S.-H., & Hyun, C.-K. (2005). Insulin sensitization of MAP kinase signaling by fibroin in insulin-resistant Hirc-B cells. *Pharmacological Research, 52*, 346–352.

Park, Y. R., Sultan, M. T., Park, H. J., Lee, J. M., Ju, H. W., Lee, O. J., Lee, D. J., Kaplan, D. L., & Park, C. H. (2018). NF-κB signaling is key in the wound healing processes of silk fibroin. *Acta Biomaterialia, 67*, 183–195.

Patel, D. K., Dutta, S. D., Ganguly, K., & Lim, K.-T. (2021). Multifunctional bioactive chitosan/cellulose nanocrystal scaffolds eradicate bacterial growth and sustain drug delivery. *International Journal of Biological Macromolecules, 170*, 178–188.

Peng, X., Yu, Y., Wang, Z., Zhang, X., Wang, J., & Liu, C. (2017). Potentiation effect of HB-EGF on facilitating wound healing via 2-N, 6-O-sulfated chitosan nanoparticles modified PLGA scaffold. *RSC Advances, 7*, 43161–43171.

Pierce, G. F., Mustoe, T. A., Altrock, B. W., Deuel, T. F., & Thomason, A. (1991). Role of platelet-derived growth factor in wound healing. *Journal of Cellular Biochemistry, 45*, 319–326.

Ramanathan, G., Seleenmary Sobhanadhas, L. S., Sekar Jeyakumar, G. F., Devi, V., Sivagnanam, U. T., & Fardim, P. (2020). Fabrication of biohybrid cellulose acetate-collagen bilayer matrices as nanofibrous spongy dressing material for wound-healing application. *Biomacromolecules, 21*, 2512–2524.

Rezvani Ghomi, E., Khalili, S., Nouri Khorasani, S., Esmaeely Neisiany, R., & Ramakrishna, S. (2019). Wound dressings: Current advances and future directions. *Journal of Applied Polymer Science, 136*, 47738.

Rezvanian, M., Ng, S.-F., Alavi, T., & Ahmad, W. (2021). In-vivo evaluation of alginate-pectin hydrogel film loaded with simvastatin for diabetic wound healing in streptozotocin-induced diabetic rats. *International Journal of Biological Macromolecules, 171*, 308–319.

Rho, C. R., Park, M.-Y., & Kang, S. (2015). Effects of granulocyte-macrophage colony-stimulating (GM-CSF) factor on corneal epithelial cells in corneal wound healing model. *PloS one, 10*, Article e0138020.

Sano, K., Ishida, Y., & Aida, T. (2018). Synthesis of anisotropic hydrogels and their applications. *Angewandte Chemie International Edition, 57*, 2532–2543.

Sen, C. K. (2019). *Human wounds and its burden: An updated compendium of estimates*. 140 Huguenot Street, 3rd Floor New: Mary Ann Liebert, Inc. publishers.

Sen, C. K. (2021). *Human wound and its burden: Updated 2020 compendium of estimates*. 140 Huguenot Street, 3rd Floor New: Mary Ann Liebert, Inc.. publishers.

Sharma, C., Dinda, A. K., Potdar, P. D., & Mishra, N. C. (2015). Fabrication of quaternary composite scaffold from silk fibroin, chitosan, gelatin, and alginate for skin regeneration. *Journal of Applied Polymer Science, 132*.

Shen, R., Xue, S., Xu, Y., Liu, Q., Feng, Z., Ren, H., Zhai, H., & Kong, F. (2020). Research progress and development demand of nanocellulose reinforced polymer composites. *Polymers, 12*, 2113.

Sugiyama, J., Chanzy, H., & Maret, G. (1992). Orientation of cellulose microcrystals by strong magnetic fields. *Macromolecules, 25*, 4232–4234.

Tang, F., Li, J., Xie, W., Mo, Y., Ouyang, L., Zhao, F., Fu, X., & Chen, X. (2021). Bioactive glass promotes the barrier functional behaviors of keratinocytes and improves the re-epithelialization in wound healing in diabetic rats. *Bioactive Materials, 6*, 3496–3506.

Thapa, R. K., Margolis, D. J., Kiick, K. L., & Sullivan, M. O. (2020). Enhanced wound healing via collagen-turnover-driven transfer of PDGF-BB gene in a murine wound model. *ACS Applied Bio Materials, 3*, 3500–3517.

Thrivikraman, G., Jagiełło, A., Lai, V. K., Johnson, S. L., Keating, M., Nelson, A., Schultz, B., Wang, C. M., Levine, A. J., & Botvinick, E. L. (2021). Cell contact guidance via sensing anisotropy of network mechanical resistance. In *Proceedings of the National Academy of Sciences 118*.

Torbet, J., Malbouyres, M., Builles, N., Justin, V., Roulet, M., Damour, O., Oldberg, Å., Ruggiero, F., & Hulmes, D. J. (2007). Orthogonal scaffold of magnetically aligned collagen lamellae for corneal stroma reconstruction. *Biomaterials, 28*, 4268–4276.

Varaprasad, K., Jayaramudu, T., Kanikireddy, V., Toro, C., & Sadiku, E. R. (2020). Alginate-based composite materials for wound dressing application: A mini review. *Carbohydrate Polymers, 236*, Article 116025.

Wang, B., Torres-Rendon, J. G., Yu, J., Zhang, Y., & Walther, A. (2015). Aligned bioinspired cellulose nanocrystal-based nanocomposites with synergetic mechanical properties and improved hygromechanical performance. *ACS Applied Materials & Interfaces, 7*, 4595–4607.

Wang, C., Chu, C., Zhao, X., Yang, Y., Hu, C., Liu, L., … Man, Y. (2021). The diameter factor of aligned membranes facilitates wound healing by promoting epithelialization in an immune way. *Bioactive Materials, 11*, 206–217.

Woodfin, A., Voisin, M.-B., & Nourshargh, S. (2007). PECAM-1: A multi-functional molecule in inflammation and vascular biology. *Arteriosclerosis, Thrombosis, and Vascular Biology, 27*, 2514–2523.

Wu, M., Zhang, Z., Liu, Z., Zhang, J., Zhang, Y., Ding, Y., Huang, T., Xiang, D., Wang, Z., & Dai, Y. (2021). Piezoelectric nanocomposites for sonodynamic bacterial elimination and wound healing. *Nano Today, 37*, Article 101104.

Xiao, X., Wang, W., Liu, D., Zhang, H., Gao, P., Geng, L., Yuan, Y., Lu, J., & Wang, Z. (2015). The promotion of angiogenesis induced by three-dimensional porous beta-tricalcium phosphate scaffold with different interconnection sizes via activation of PI3K/Akt pathways. *Scientific Reports, 5*, 1–11.

Xing, W., Guo, W., Zou, C.-H., Fu, T.-T., Li, X.-Y., Zhu, M., Qi, J.-H., Song, J., Dong, C.-H., & Li, Z. (2015). Acemannan accelerates cell proliferation and skin wound healing through AKT/mTOR signaling pathway. *Journal of Dermatological Science, 79*, 101–109.

Xing, W., & Tang, Y. (2021). On mechanical properties of nanocomposite hydrogels: Searching for superior properties. *NanoMaterials Science, 2021*, 1–14.

Yu, J. R., Navarro, J., Coburn, J. C., Mahadik, B., Molnar, J., Holmes, J. H., IV, Nam, A. J., & Fisher, J. P. (2019). Current and future perspectives on skin tissue engineering: Key features of biomedical research, translational assessment, and clinical application. *Advanced Healthcare Materials, 8*, 1801471.

Yu, M., Chen, Z., Guo, W., Wang, J., Feng, Y., Kong, X., & Hong, Z. (2015). Specifically targeted delivery of protein to phagocytic macrophages. *International Journal of Nanomedicine, 10*, 1743.

Yussof, S. J. M., Omar, E., Pai, D. R., & Sood, S. (2012). Cellular events and biomarkers of wound healing. *Indian Journal of Plastic Surgery, 45*, 220–228.

Zarket, B. C., Wang, H., Subraveti, S. N., & Raghavan, S. R. (2021). Multilayer tubes that constrict, dilate, and curl in response to stimuli. *Soft Matter, 17*, 4180–4190.

Zhang, H., Weström, S., Kappelin, P., Virtanen, M., Vahlquist, A., & Törmä, H. (2021). Exploration of novel candidate genes involved in epidermal keratinocyte differentiation and skin barrier repair in man. *Differentiation, 119*, 19–27.

Zhou, K., Li, Y., Zhang, L., Jin, L., Yuan, F., Tan, J., Yuan, G., & Pei, J. (2021a). Nano-micrometer surface roughness gradients reveal topographical influences on differentiating responses of vascular cells on biodegradable magnesium. *Bioactive Materials, 6*, 262–272.

Zhou, Y., Gao, L., Peng, J., Xing, M., Han, Y., Wang, X., Xu, Y., & Chang, J. (2018). Bioglass activated albumin hydrogels for wound healing. *Advanced Healthcare Materials, 7*, 1800144.

Zhou, Z., Vázquez-González, M., & Willner, I. (2021b). Stimuli-responsive metal–organic framework nanoparticles for controlled drug delivery and medical applications. *Chemical Society Reviews, 50*, 4541–4563.